Towards Optical Detection of Phonons in Surface Acoustic Wave Resonators

Doedes, Yasmin

Towards Optical Detection of Thermal Phonons in Surface Acoustic Wave Resonators
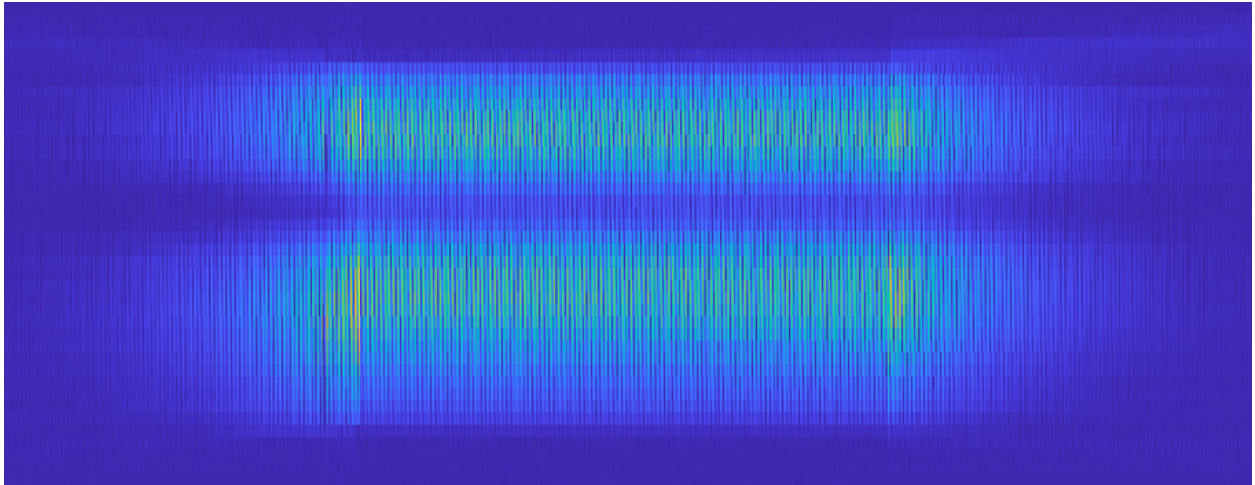
THESIS

submitted in partial fulfillment of the
requirements for the degree of

MASTER OF SCIENCE
in
PHYSICS

Author :	Yasmin Charlotte Doedes
Student ID :	s2028638
Supervisor :	Matteo Fisicaro, MSc
	Dr. Wolfgang Löffler
Second corrector :	Dr. Alexandre Morin

Leiden, The Netherlands, July 3, 2023

Towards Optical Detection of Thermal Phonons in Surface Acoustic Wave Resonators

Yasmin Charlotte Doedes

Leiden Institute of Physics, Leiden University
P.O. Box 9500, 2300 RA Leiden, The Netherlands

July 3, 2023

Abstract

Surface acoustic wave (SAW) resonators can confine and enhance the displacement associated with SAW phonons. SAW resonators are useful in quantum technology, where they are used to enhance the coupling between a single phonon and a semiconductor quantum dot (QD). In this thesis, the fabrication process of SAW resonators on GaAs with acoustic mirrors based on aluminum Bragg reflectors, and an investigation into the relation between the finesse of a resonator and the thickness of the aluminum mirrors are detailed. For this purpose, three resonators identical in design apart from the thickness of their aluminum mirrors (35 nm, 50 nm, and 100 nm) are fabricated. The finesse of these resonators is derived by examining their acoustic resonance spectra and displacement maps. Both types of measurements are performed with a fiber-based scanning Michelson interferometer. It is found that losses associated with the resonator limit the finesse. The maximal finesse is found to be $\mathcal{F} \approx 11$ for the 100 nm resonator. Based on the measurement results, it is hypothesized that reducing the resonator length will lead to a decrease in propagation loss, thereby raising the upper limit of the finesse. This project has been a step towards the optical detection of thermal phonons, with its final goal to detect single phonons.

Contents

Chapter 1

Introduction

In this thesis, the development of surface acoustic wave (SAW) resonators on gallium arsenide (GaAs), with the intention of detecting thermal phonons in the future, will be detailed. The main objective of this research is to investigate how the resonator design, specifically the metal thickness (along the z-direction), relates to the finesse. The displacement associated with thermal phonons can be enhanced, and thus be more easily detectable by increasing the finesse. Prior to discussing acoustic resonators, SAWs need to be touched upon. This introduction will briefly go into SAWs and their characteristics, the current and prospected applications of SAW resonators, with an eye on their use in quantum technology.

SAWs are waves that travel on the surface of a material. There are various types of SAWs, but in this research we will only consider Rayleigh waves. Therefore, the terms 'SAW' and 'Rayleigh wave' will be used interchangeably throughout this thesis. Figure 1.1 depicts a traveling SAW. This wave has a displacement along both the transverse (along the z-direction) and longitudinal direction, with different amplitude and phase. In particular the transverse displacement has the biggest amplitude, and has a $\pi/2$ phase difference with respect to the longitudinal one. This causes a volume element in the material to undergo an elliptical motion as the wave passes by. Both displacement components decay exponentially with distance into the material, although the exact decay rate differs [1, Ch. 5]. Consequently, the displacement is confined to roughly one wavelength into the material.
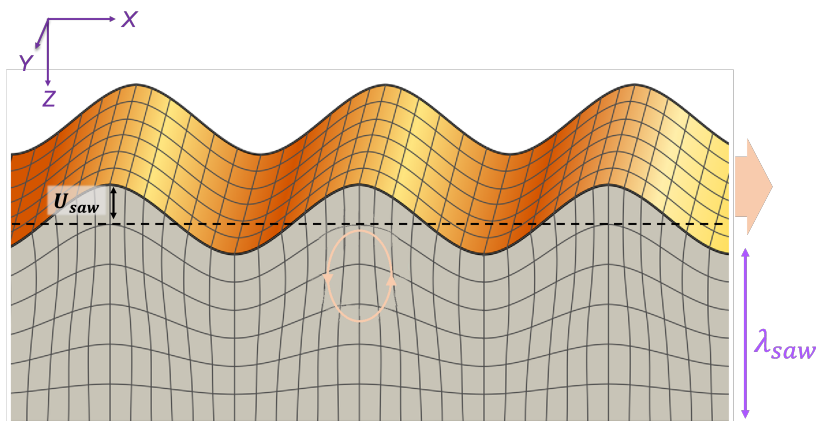
Figure 1.1: Rayleigh wave Surface acoustic waves (SAWs) with displacement in both the longitudinal and transverse direction are called Rayleigh waves. The right-pointing arrow indicates the travel direction of the wave. The ellipse with arrows depicts the movement of particles in the substrate as a result of the traveling wave. The displacement decays exponentially into the substrate and is confined to approximately one wavelength λ_{saw} into the substrate. The SAW displacement U_{saw} is defined with respect to the wave-free substrate surface. Adapted from [2].

SAW resonators in acoustics are analogous to cavities in optics. Inside SAW resonators, SAWs are confined by two acoustic mirrors. The acoustic mirrors are a type of Bragg reflectors. Under resonant conditions, the SAWs interfere constructively. SAW resonators have been broadly used in technology, for example as biological and chemical sensors [3] and filters in mobile communication technology [4].

Another application of SAW resonators is found in quantum technology. Phonons, in particular SAW phonons, can effectively couple to quantum dots (QDs). The displacement that is associated with phonons, is caused by stress and strain in the substrate. In piezoelectric materials, the displacement is accompanied by an electric field as well. Both this stress and strain [5], and this electric field can couple to a QD. Of course, this coupling to a QD is only useful to quantum technology when single phonons can be isolated and coupled. Research has shown that it is possible to excite single phonons with an interdigital transducer that is coupled to a superconducting qubit [6]. A single phonon can more easily interact with a QD when both are placed inside an acoustic resonator, since this enhances the phonon displacement and thus the coupling.

Through the coupling mechanism described above, phonons seem to be promising carriers of quantum information [7–11]. Therefore, phonons inside acoustic resonators are an interesting topic of study. One method of investigating phonons in acoustic resonators, is by detecting their displacement. Since the acoustic field is mostly confined in between the two mirrors, to image the entire region, one needs a probe that can locally measure the displacement and that can be swept spatially over the entire region. The displacement for electrically excited SAW phonons is in the order of 10-100 pm [12]. In order to measure such small displacements, many techniques have been used such as optical interferometric measurements [13–15], X-ray diffraction [16, 17] and atomic force microscopy [18, 19]. In this research, a fiber-based scanning Michelson interferometer is used to detect SAWs and to image the SAW field inside acoustic resonators.

This thesis will focus on the optical detection of electrically excited phonons inside acoustic resonators. As will be elaborated on in Sec. 2.3, the displacement of single phonons and thermal phonons in acoustic resonators is extremely small. A first step is therefore to detect a larger displacement: electrically excited phonons. Chapter 2 will provide a theoretical description of interdigital transducers, which are used to electrically generate SAW phonons, and SAW resonators consisting of two acoustic Bragg reflectors. The next chapter, 3, will describe the scanning Michelson interferometer that is used to characterize acoustic resonators. Two types of data can be obtained with this setup: acoustic resonance spectra and displacement maps. These two types of measurements will be introduced with reference to the measurement results of a generic sample. Then, in chapter 4, the fabrication process of acoustic resonators will be explained. All resonators discussed in this thesis are fabricated by electron-beam lithography and electron-beam metal evaporation. Also, the design considerations that contribute to optimizing the finesse and allowing for measurement with the scanning Michelson interferometer, will be detailed in chapter 4. In the final chapter, 5, an analysis of the acoustic resonance spectra and displacement maps of three resonators (resonators B35, B50, and B100) will be presented. These three resonators are identical, except for their metal thickness. The finesse and mirror quality in relation to the metal thickness will be examined. In chapter 6, the findings will be summarized and experiments to further investigate the influence of metal thickness on the finesse will be suggested. Lastly, the steps from the current state to detection of thermal phonons will be touched upon.

Chapter 2

Theory

2.1 Interdigital transducers for SAW creation

This research is about the detection of confined surface acoustic waves (SAWs) using a scanning Michelson interferometer. Despite the ultimate goal being the detection of single and thermal SAW phonons, the SAWs that are detected in this research are electrically generated. The reason is the limited sensitivity of the current setup.
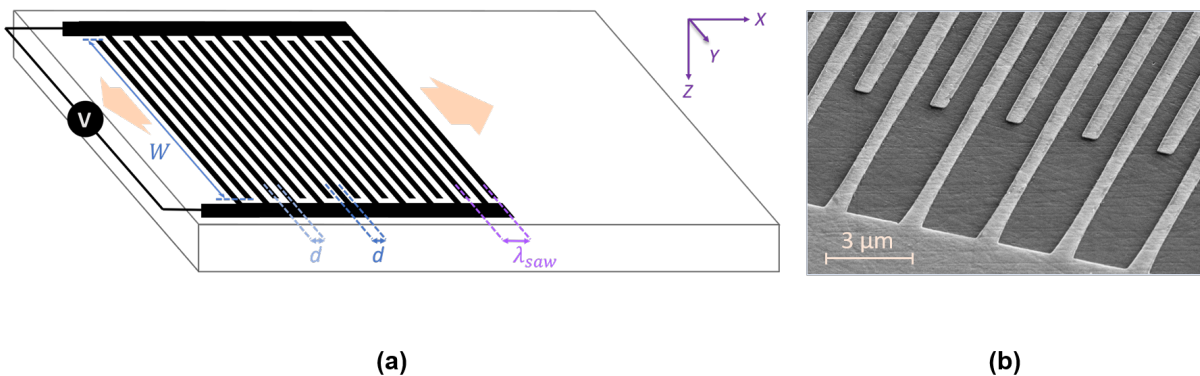

Figure 2.1: Interdigital transducer (IDT) An IDT in its simplest form consists of two combs of interdigitated electrodes patterned on a piezoelectric material. **(a)**: A diagram of an IDT with characteristic lengths. The number of finger pairs for this schematic is $N_f = 10$. The IDT is additionally characterized by the distance d, which is both the distance from the center of one finger to the center of an adjacent finger and the distance from the center of one gap to the center of an adjacent gap. The resonant wavelength of an IDT with inter-finger distance d is $\lambda_{saw} = 2d$. The finger overlap in the y-direction is referred to as the acoustic aperture W. One of the electrode combs is connected to an RF generator. The generated SAWs move outward in the positive and negative x-directions (indicated by the orange arrows). **(b)**: A scanning electron microscope (SEM) image of an IDT on GaAs, with $d = 2.8$ µm.

Interdigital transducers (IDTs) are nanofabricated devices that are used for the excitation of SAWs. They consist of two interdigitated combs of electrodes patterned on a piezoelectric material. Piezoelectricity is a requisite, as the creation of SAWs with IDTs is based on the inverse piezoelectric effect: when an electric field is applied to a piezoelectric material, a deformation of the material will follow. The most basic (and frequently used) IDT design is depicted in Fig. 2.1. An IDT is characterized by the number of finger pairs N_f and a set of distances: the acoustic aperture W which is the overlap of the fingers in the y-direction, and the center-to-center distance between two adjacent fingers d. When the finger width equals the gap width, the center-to-center distance between two adjacent gaps will also be d. The wavelength of the generated SAW is given by $\lambda_{saw} = 2d$. The acoustic aperture is typically at least a hundred times larger than the wavelength, $W > 100\lambda_{saw}$, to

limit divergence of the generated waves [12, Ch. 2]. When applying a voltage to one of the combs (the other comb is usually grounded), every finger pair will create SAWs. Because of the periodicity of the finger pairs, these generated waves will interfere constructively giving rise to a larger displacement.

For this research gallium arsenide (GaAs) in (001)-cut and in [110]-direction is used as the piezoelectric substrate. The IDT design from Fig. 2.1, that is also used for this research, generates SAWs in both the positive and negative x-direction. Other more involved IDT designs exist that limit the wave generation to one direction [12, Ch. 2].
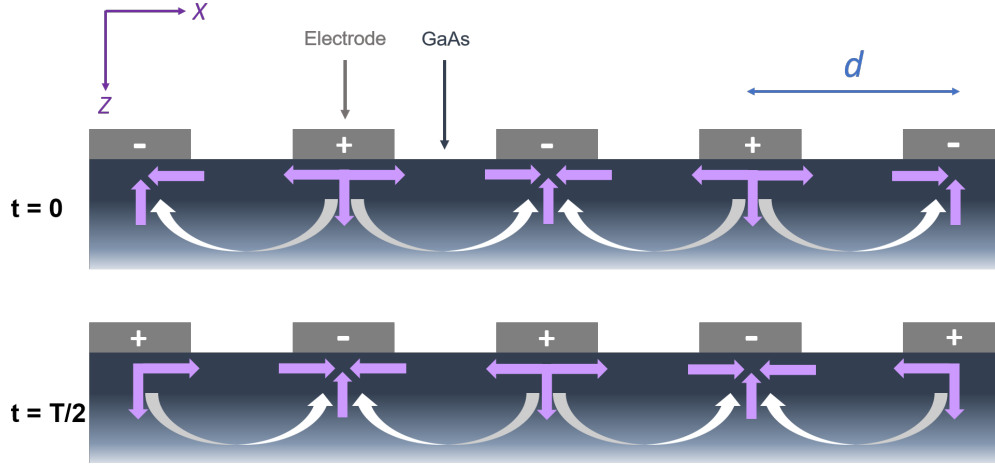
Figure 2.2: Field lines and substrate deformation The charge (+ or -) of five IDT electrodes is shown at two instances in time. The two instances are separated by half a period (T/2) of the AC voltage. Underneath the electrodes, in the piezoelectric material, the electric field lines arising from the charged electrodes are shown in white. The displacement of the material following from the inverse piezoelectric effect is shown in purple. The indicated charges (+ and –) are relative, as in practice, one of the finger combs is grounded.

An AC voltage with frequency f_{AC} is applied to one of the electrode combs whilst the other comb is grounded. As a result, electric fields and displacements as indicated in Fig. 2.2 are generated between the fingers. The sign of the fields switches with frequency f_{AC}. Depending on the field strength and sign, a certain strain will arise on the material surface. Underneath fingers where field lines diverge, the material will be compressed horizontally. Conversely, underneath fingers where field lines converge, the material will be expanded horizontally. The created regions of compression and expansion (acoustic waves) move outward with a velocity depending on the material. For GaAs in the mentioned cut and orientation, the SAW speed is approximately $v_{saw} = 2860$ m/s. Associated with the created SAWs is a wavelength $\lambda_{saw} = 2d$ and a frequency $f_{saw} = v_{saw}/2d$. When the SAW frequency matches the AC frequency, $f_{AC} = f_{saw}$, the action of the individual fingers combined will cause constructive interference of the SAW. This frequency is referred to as the resonant frequency f_0. However, this only explains the origin of the longitudinal component of the Rayleigh wave. The transverse displacement simply follows from the requirement that the volume must stay constant: compression in the horizontal direction leads to expansion in the vertical direction. The longitudinal displacement is maximal halfway between two electrodes, whereas the transverse displacement is maximal underneath electrodes. This difference in the location of maximal displacement also clarifies the origin of the $\pi/2$ phase difference between the transverse and longitudinal displacement components of a Rayleigh wave.

A second IDT can be used to detect the SAWs. In this case, the working principle is based on the direct piezoelectric effect: a traveling displacement in a piezoelectric material is accompanied by an electric field. This oscillating electric potential is detected by electrodes as the SAW passes underneath. But that is not the only effect of a passing SAW underneath an IDT. A secondary ef-

fect is re-emission: the voltage that is induced across the fingers causes the generation of secondary SAWs through the inverse piezoelectric effect. Another secondary effect is partial reflection at the electrode edges. There is a mechanical impedance mismatch on the surface as a wave moves from the bare substrate to the metallized substrate. This impedance mismatch results in a partial reflection.

Also, it has to be noted that SAWs are not the only acoustic waves that are generated (and detected) by IDTs. Other elastic waves, such as bulk acoustic waves (BAWs), will be present as well. More information can be found in Sec. 2.2.1.

2.1.1   Frequency response

As mentioned above, when the frequency of the applied voltage matches the intended SAW frequency, $f_{AC} = f_{saw}$, the resonance condition is met and the SAWs that are created by the IDT fingers will interfere constructively, creating a wave with maximal displacement. When f_{AC} slightly deviates from f_{saw}, the constructive interference diminishes and the signal strength reduces. The frequency response of an IDT follows from the impulse response model [12, Ch. 2]. The acoustic resonance spectrum follows a sinc function:

$$\phi(f) \propto \sin(X)/X$$
$$X = \pi N_f \frac{f - f_0}{f_0} \tag{2.1}$$

In the equation above, ϕ is the electric potential in the piezoelectric material. The resultant material displacement also depends on the strength of the voltage that is applied to the electrodes and piezoelectric material constants. The frequency f refers to the frequency of the AC voltage, earlier called f_{AC}. Associated with this frequency response is the 3dB bandwidth:

$$\frac{\Delta f}{f_0} \approx \frac{0.885}{N_f} \tag{2.2}$$

As visible in Eq. 2.2, the range of frequencies that can be excited by an IDT gets narrower with an increase in the number of finger pairs N_f.

2.2   Acoustic resonators for SAW confinement

IDTs create traveling SAWs. For certain applications, such as sensing and filtering, the SAWs must be confined to a small volume. When confined, the displacement of the SAW increases. This is also advantageous when attempting to measure thermal SAW phonons. Confining SAWs in acoustic resonators is analogous to confining electromagnetic waves in a Fabry-Pérot cavity. In a Fabry-Pérot cavity, the waves are confined by mirrors with high reflectivity. An acoustic resonator is constructed with acoustic mirrors, ideally with a high reflectivity as well. In Sec. 2.1 it was mentioned that IDTs act as low-quality mirrors: a secondary effect of a SAW incoming on an IDT is partial reflection. For that reason, acoustic mirrors are in design very similar to IDTs: an acoustic mirror consists of an array of shorted electrodes. The number of electrodes is indicated by N_m. Figure 2.3 shows a schematic of the simplest acoustic resonator design. The spacing and width of the electrodes in the acoustic mirrors d matches the spacing and width of the IDT fingers. In Fig. 2.3, the number of electrodes in the acoustic mirrors equals 11, but in practice, N_m should be at least an order of magnitude larger to achieve moderate reflection.

Prior to describing some characteristics of acoustic resonators, the mechanism by which acoustic mirrors reflect SAWs needs to be touched upon. The primary reflection mechanism has already been briefly mentioned: mechanical impedance mismatch between bare and metallized substrate. When there is metal on top of the substrate, there will be mass loading. When a traveling SAW encounters the first electrode of a mirror, there is a change in wave velocity because of this mass loading. This
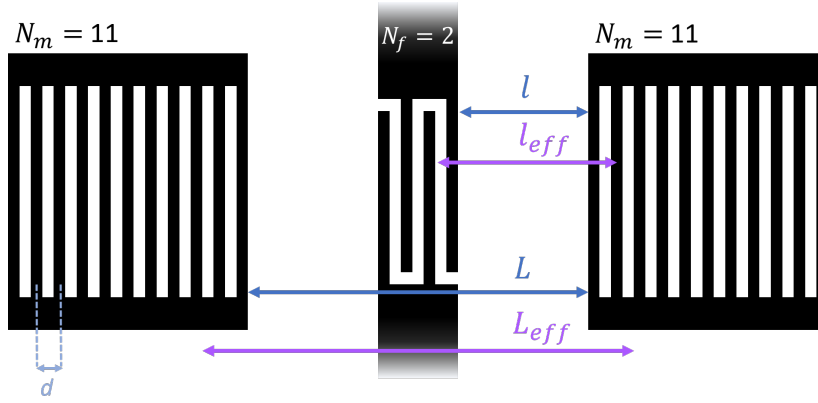
Figure 2.3: An acoustic resonator with an IDT An acoustic resonator consists of two acoustic mirrors and for driving and detection one or two IDTs, all patterned on a piezoelectric material. The acoustic mirrors consist of N_m shorted electrodes. The electrode width and spacing d equals the IDT finger width and spacing. SAWs generated by the IDT form standing waves between the two mirrors. The resonator length L is the distance between the two innermost mirror electrodes. In practice, the SAWs slightly penetrate the mirrors, leading to an effective resonator length, L_{eff}. Because an IDT acts like an acoustic mirror with lower reflectivity compared to an actual acoustic mirror, two effective resonators can be identified. Also for an effective resonator, there is an associated length, l, and effective length, l_{eff}.

is analogous to an electromagnetic wave encountering a different medium: there will be a change in refractive index and thus the wave velocity. The acoustic mirrors impose an electrical impedance mismatch as well, which also contributes to the reflection of the waves.

The repetition of electrodes in the acoustic mirrors leads to consecutive partial reflections. This means that a SAW penetrates the acoustic mirror to some extent before being fully reflected. Therefore, an effective cavity length L_{eff} can be defined. The effective resonator length is the mirror separation when the reflecting arrays would be replaced by an idealized thin mirror. This is analogous to Bragg reflectors in optics [20].

A theoretical expression for the single-finger amplitude reflection coefficient r_e of an IDT finger reads [12, Ch. 2]:

$$r_e = iR_p \frac{K_R^2}{2} + iR_m \frac{h}{\lambda_{saw}} \quad \text{when} \quad \frac{h}{\lambda} << 0.002 \tag{2.3}$$

Note that the expression above is for IDT fingers. However, mirror fingers are expected to behave similarly. The first contribution to the reflection comes from the electrical impedance mismatch, and the second contribution comes from the mechanical impedance mismatch. R_p is a function that depends on array design. For the design depicted in Fig. 2.3, $R_p = $ -0.72 [21]. Moreover, $K_R^2 = 0.07\%$ [3] is the electromechanical coupling constant for GaAs. R_m is another function that depends on the material properties of both the substrate and electrodes. Finally, h/λ is the ratio of the electrode height to the SAW wavelength. For the designs discussed in this thesis, $h/\lambda > 0.002$. This means that the true single-finger reflectivity will differ from the theoretical value. Also, the electrical contribution to the total reflectivity is less than 1% for the discussed designs [21, table 6.3].

After an examination of the reflection mechanisms, other resonator characteristics such as the resonances can be described. A resonator has multiple resonances. In terms of frequency, the resonances f_{res} are given by:

$$f_{res} = n \frac{v_{saw}}{2L_{eff}} \tag{2.4}$$

In the equation above, n is a positive integer. The free spectral range Δf_{FSR} is defined as the

frequency separation between two consecutive resonances:

$$\Delta f_{FSR} = \frac{v_{saw}}{2L_{eff}} \tag{2.5}$$

Analogous to a Fabry-Pérot cavity in optics, the performance of an acoustic resonator can be characterized by both the quality factor Q and the finesse $\mathcal{F}$. The quality factor is defined as the ratio of the resonance frequency to the full width half maximum (FWHM) Δf_{FWHM}. The FWHM indicates the width of the resonance peak.

$$Q = \frac{f_{res}}{\Delta f_{FWHM}} \tag{2.6}$$

The quality factor is a measure of how long a wave can be confined inside a resonator. This means that the quality factor is dependent on the effective length and the mirror reflectivity. The finesse can be used to quantify the quality of a resonator as well. In a lossless scenario, the finesse solely depends on the reflectivity.

$$\mathcal{F} = \frac{\Delta f_{FSR}}{\Delta f_{FWHM}}$$
$$\mathcal{F}_{lossless} = \frac{\pi\sqrt{|r|}}{1 - |r|} \tag{2.7}$$

In the equation above, r is the mirror reflectivity. The quality factor and finesse are related by: $Q = n\mathcal{F}$. A high-finesse resonator is useful for enhancing weak signals, for example thermal phonons. The total power of thermal noise in a resonator is conserved, regardless of the finesse. Increasing the finesse leads to a sharper peak in the power spectral density around the resonance frequency. A sharper peak is beneficial for the signal-to-noise ratio.

2.2.1 SAW loss mechanisms

The creation, propagation, and reflection of SAWs are all associated with loss mechanisms [12, Ch. 2]. First of all, when creating SAWs with an IDT not all energy is converted to SAWs: as a side effect, BAWs are generated. Also, when SAWs travel in between the two acoustic mirrors, the beam widens by diffraction. This divergence is limited when the acoustic aperture is much larger than the wavelength of the generated waves. Furthermore, imperfections in the metal deposition of the IDT lead to irregular phase fronts. Uneven metal thickness along one finger leads uneven mass loading and thus uneven wave speeds underneath that finger. Also, imperfections in the lengths of the IDT fingers leads to phase speed variations. This effect, however, is small for substrates with low electromechanical coupling, K_R^2. For GaAs, this constant is low and irregular phase fronts are of no large concern.

The reflection of SAWs on acoustic mirror electrodes is also subject to loss. The impedance mismatch between bare and metallized substrate does not only lead to reflection in the opposite direction. Part of the incoming SAWs are also converted into BAWs. This conversion is dependent on the degree of mass loading, and thus the thickness of the metal fingers. The influence of the metal thickness on the performance of the resonator will be investigated in chapter 5.

Other general losses, associated with both creation and reflection are acoustic attenuation by deformation of the metal and coupling of SAWs to thermal phonons.

2.3   Single and thermal SAW phonons

As mentioned in the introduction (chapter 1), single phonons are promising as carriers of quantum information. When confined in an acoustic resonator, single phonons can interact with a variety of

systems, for example quantum dots. Because of this application, it is worthwhile to elaborate on single phonons. The displacement associated with a single phonon is approximated by the zero-point mechanical motion [7]:

$$U_0 \approx \sqrt{\frac{\hbar}{2\rho v_{saw} A}} \tag{2.8}$$

In the equation above, ρ is the mass density of the substrate ($\rho_{GaAs} = 5.32 \text{ g/cm}^3$) and A is the resonator area. Resonator areas of $200\lambda_{saw}^2$ have been demonstrated to be achievable [7]. For this confinement, the single phonon displacement on GaAs is $U_0 \approx 0.05$ fm. This displacement is extremely small and therefore challenging to detect. To simplify the task it is sensible to focus first on a displacement that is slightly larger: thermal phonon displacement.

The interferometric setup that will be presented in this thesis (chapter 3) operates at room temperature. Moreover, the open microcavity that is envisioned to be used in further research, can operate at room temperature as well. A temperature above the ground-state temperature leads to thermal noise in the SAW resonator. When modelling the acoustic resonator as a harmonic oscillator, the thermal displacement is derived in [22].
The power spectral density of the thermal noise is given by S_{FF}. Because thermal noise is random, it follows a white power spectral density:

$$S_{FF} = 4k_B T m_{eff} \gamma \tag{2.9}$$

In the equation above, m_{eff} is the effective mass of the resonator, and γ is the damping rate. S_{xx} is the power spectral density of the resonator displacement. The displacement occurs in response to the thermal noise. S_{xx} and S_{FF} are related via the mechanical susceptibility $\chi(\omega)$:

$$S_{xx}(\omega) = |\chi(\omega)|^2 S_{FF}$$
$$S_{xx}(\omega) = \frac{k_B T \gamma}{m_{eff} \omega_0^2} \frac{1}{(\omega - \omega_0)^2 + (\gamma/2)^2} \tag{2.10}$$

ω_0 is the angular resonance frequency. Notice that contrary to S_{FF}, S_{xx} is dependant on the angular frequency ω. S_{xx} peaks sharply around the resonance frequency. Finally, the thermal phonon displacement is found by:

$$U_{th}^2 = \langle x^2 \rangle = \int S_{xx}(\omega) d\omega = \frac{k_B T}{m_{eff} \omega^2} \tag{2.11}$$

Computing the thermal displacement according to Eq. 2.11, requires an expression for the effective mass. The effective mass is the mass of the resonator when it would be modeled as an oscillating point-like mass. It depends on the material displacement associated with the standing SAW and the substrate mass density [23]. When the substrate displacement is approximated to be sinusoidal with an amplitude that exponentially decays with penetration into the material, the following expression can be derived:

$$\left.\begin{array}{l} m_{eff} = n_x n_y \rho \int d\vec{r} |d_z(\vec{r})|^2 \\ d_z(x,z) \approx e^{-z/\lambda_{saw}} sin\left(\frac{2\pi}{\lambda_{saw}} x\right) \\ x = [0, \lambda_{saw}], \ y = [0, \lambda_{saw}], \ z = [0, \infty] \end{array}\right\} \quad m_{eff} = n_x n_y \rho \frac{\lambda_{saw}^3}{4} \tag{2.12}$$

n_x and n_y are the resonator dimension in the x and y dimensions in terms of the number of wavelengths. $d_z(x,y)$ is the substrate displacement in the z-direction. x, y, and z are defined as in Fig. 1.1. For 1 GHz SAWs on GaAs, in a resonator with area of $200\lambda_{saw}^2$, at room temperature, the thermal displacement is $U_{th} \approx 4$ fm. Although still very small, this displacement is two orders of magnitude larger than the single phonon displacement for the same resonator size.

Chapter 3

Scanning Michelson Interferometer

This project aims to optically detect SAW phonons that are confined inside acoustic resonators. The optical detection setup that is used, is a scanning Michelson interferometer. Because of sensitivity restrictions, the interferometer can only be used to measure electrically excited phonons and not thermal phonons. The noise analysis in Sec. 3.3 will further discuss the sensitivity. Despite the limited sensitivity, the interferometer is essential as it can be used to perform a general characterization of an acoustic resonator: both two-dimensional displacement maps and acoustic resonance spectra can be obtained.

3.1 Experimental setup

Figure 3.1 depicts the Michelson interferometer setup that is used to obtain two-dimensional displacement maps and acoustic resonance spectra of acoustic resonator samples. An infrared laser with an approximate wavelength of 1 µm is connected to a polarization-maintaining, 50:50 fiber beam splitter. In both output arms of the beam splitter (A and B), the laser light is coupled to free space, reflected by a mirror and then coupled back into the fiber. In arm A, the acoustic resonator is mounted on an XYZ stage. Movement in the X- and Y-directions allows for the laser to be scanned over the surface of the sample. The laser beam is focused onto the sample using an aspheric lens with focal length f = 2.75 mm. The acoustic resonator samples are fabricated on GaAs; a material with roughly 30% reflectivity at the wavelength $\lambda = 1$ µm. In arm B, there is a small mirror on a piezo. Through connection with a PID lockbox and piezo amplifier, this piezo stabilizes the interferometer up to a few kHz. Because the acoustic resonators are designed for GHz surface waves, the piezo vibrations will have no impact on the interference signal caused by the surface waves. The recombined in-fiber signal is sent through another beam splitter. A slow photodiode (slow PD) that is used as input for the PID lockbox, captures part of the signal, while the other part of the signal is detected by a radio-frequency photodiode (RF PD). This photodiode is connected to a spectrum analyzer to record the small GHz modulation.

Before the recording of a displacement map, the sample needs to be aligned. In order to align the sample, the signal in the sample arm is split using a pellicle beam splitter. The faint signal is projected onto a CCD camera. The light scattered by the metal structures on the GaAs, allows for imaging of the sample. Moreover, to ensure optimal visibility, the laser power in both arms is matched. This is done by slightly detuning the free space-to-fiber coupling in the arm B. The advantage of a fiber beam splitter as opposed to a free space beam splitter is the fact that the fiber beam splitter is an effective mode selector. Because the fiber only allows a single laser mode to enter, it is ensured that the two signals fully overlap. Hence, small alignment imperfections in either arm are compensated for, at the slight expense of signal strength.
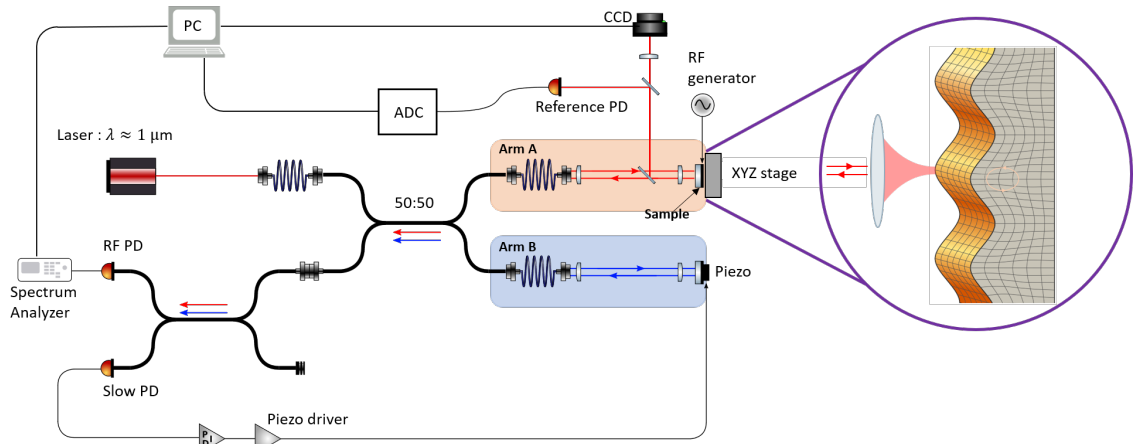
Figure 3.1: Experimental set-up The scanning Michelson interferometer setup is used for obtaining displacement maps and acoustic resonance spectra of acoustic resonators. An infrared (IR) laser goes through a polarization maintaining, 50:50 fiber beamsplitter. The acoustic resonator (the sample) is placed in arm A. The sample is mounted on an XYZ-stage, such that the laser beam can be focused onto the sample, and the sample can be scanned in the X- and Y-directions. In arm B, a mirror is mounted on a piezo in order to stabalize the signal. The recombined signal is split by another fiber beamsplitter. Part of the signal is recorded by a radio frequency photodiode (RF PD) and spectrum analyzer. The other part of the signal is fed into a slow photodiode (slow PD) that is connected to a PID and piezo driver. In arm A, there is a pellicle beam splitter that directs a faint signal to a CCD and reference photodiode (reference PD). The CCD is used to image the sample during alignment. The reference photodiode (reference PD) in combination with an analog-to-digital converter (ADC) is used to measure the DC power reflected by the sample. An IDT on the sample is connected to a radiofrequency generator (RF generator) such that SAWs can be excited. The Rayleigh wave picture (right) is adapted from [2].

Lastly, a reference photodiode (reference PD) is used to record the DC power reflected while the sample is scanned. Parts of the sample that are patterned with metal will reflect more laser light compared to bare GaAs. In this way, a map of the metal structures can be constructed.

3.2   Calibration

As mentioned, the displacement maps are constructed from the response of the RF PD and spectrum analyzer. The RF PD detects AC laser power and transforms it into a voltage. By calibrating the interferometer, this voltage can be converted into a displacement, thereby creating the displacement map. C is the conversion factor between the voltage measured by the RF PD and the displacement on the substrate. The objective is to understand how a change in the voltage recorded by the RF PD translates to a displacement on the substrate. A longitudinal displacement of the GaAs substrate will change the length of arm A and therefore will cause a phase difference between arms A and B. It is more straightforward to relate a change in voltage on the slow PD to a displacement, as this PD can measure the low frequency interference pattern created by scanning the piezo over few interference fringes (as shown in Fig. 3.2). After establishing this relation (C_1), a conversion between RF PD and slow PD (C_2) can be made.

When the piezo is scanned over some length ΔL, the voltage recorded by the slow PD shows an interference pattern, see Fig. 3.2. As stated, the PID is used to stabilize arm B. By locking the length of arm B at half the interference fringe (purple dot in 3.2), the interferometer will have

optimal sensitivity. The inverse of the slope at the lock point, $C_1 = \partial(\Delta L)/\partial V_{slow}$, is the conversion factor between the voltage on the slow PD and the displacement on the substrate.
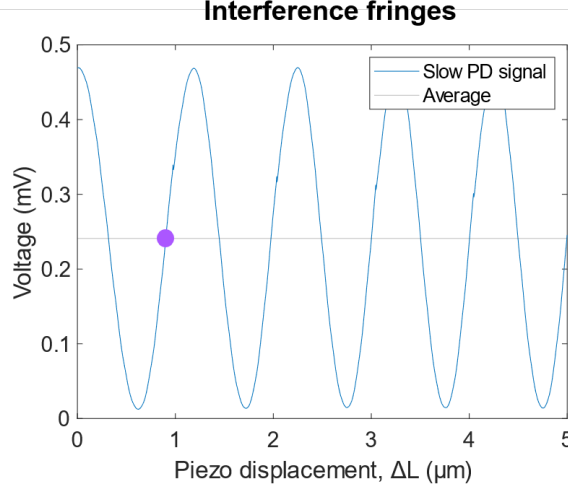
Figure 3.2: Interference fringes When the piezo is scanned, the time trace of the voltage recorded by the slow PD shows an interference pattern. Voltage vs. time yields the same plot as voltage vs. the length ΔL over which the piezo has scanned. The visibility is nearly 100% as the minimum voltage approaches zero. Locking the length of arm B at half the fringe (indicated by purple dot) yields the highest interferometric sensitivity because at this point, a change in arm length will result in the highest possible change in voltage.

Finally, a conversion between the slow- and RF PD voltage is made. From the manual it is known that the conversion between detected power and voltage output for the slow PD is $c_{slow} = V_{slow}/P_{laser} \approx 980$ V/W. To find the same conversion factor for the RF PD, $c_{RF} = V_{RF}/P_{laser}$, an experiment is performed: the laser intensity is modulated by a few MHz and shined directly on both PDs, recording the voltage over time. Using c_{slow}, the original power signal can be reconstructed. By comparing this signal to the voltage recorded by the RF PD, c_{RF} is determined. The transformation between voltage recorded by the slow and RF PD is then given by $C_2 = c_{slow}/c_{RF}$. Combining C_1 and C_2 gives rise to C, which relates a change in voltage on the RF PD to a displacement caused by a SAW. For laser light with a wavelength of 1 µm, C is given by:

$$C = \frac{\Delta d_{saw}}{\Delta V_{RF}} = C_1 \cdot C_2 = \frac{\partial(\Delta L)}{\partial V_{slow}} \cdot \frac{V_{slow}}{V_{RF}} \approx 0.38 \text{ pm/µV} \tag{3.1}$$

3.3 Noise analysis

The displacement maps that are created with the interferometer are subject to several sources of noise. First of all, the laser that is used to probe the sample is not perfectly stable. The laser intensity fluctuates slightly in time but this is of no concern as the fluctuations will be present throughout the entire setup. The laser wavelength possibly has modulations, but these will not be in the GHz range and therefore can be disregarded as well. Moreover, environmental vibrations are also not in the range of the SAW frequency and require no consideration.

The primary sources of noise are the RF PD and the spectrum analyzer. When performing a measurement, these two sources primarily make up the electronic noise. The electric noise level is determined to be -130 dBm or 70 nV. This amounts to a displacement of 24.5 fm.

Depending on the type of measurement, thermal phonons on the substrate can also be considered noise. Section 2.3 derives the displacement caused by thermal phonons. Assuming room temperature ($T = 293$ K) and a SAW confinement of 150λ by 100λ (this is the resonator size used in chapter 5, see Fig. 5.1), the displacement caused by thermal phonons on GaAs is $U_{th} \approx 0.5$ fm. This is very small compared to the overall noise. Consequently, it is not possible to detect thermal phonons with

the current setup. A more sensitive instrument, such as an optical microcavity, is required, as well as a smaller resonator.

3.4   Measurement results

In this section, the measurement results (acoustic resonance spectra and displacement map) of sample A will be presented. Sample A is an acoustic resonator consisting of two mirrors and two IDTs. This resonator design is of no particular interest when creating acoustic resonators for thermal phonon detection. In fact, this resonator is relatively complex because it consists of three sub-resonators. However, a brief analysis of these measurement results will set a baseline for interpreting measurement results of other devices that will be introduced in chapter 5. Because of the sample complexity of sample A, a detailed analysis is beyond the scope of this research.
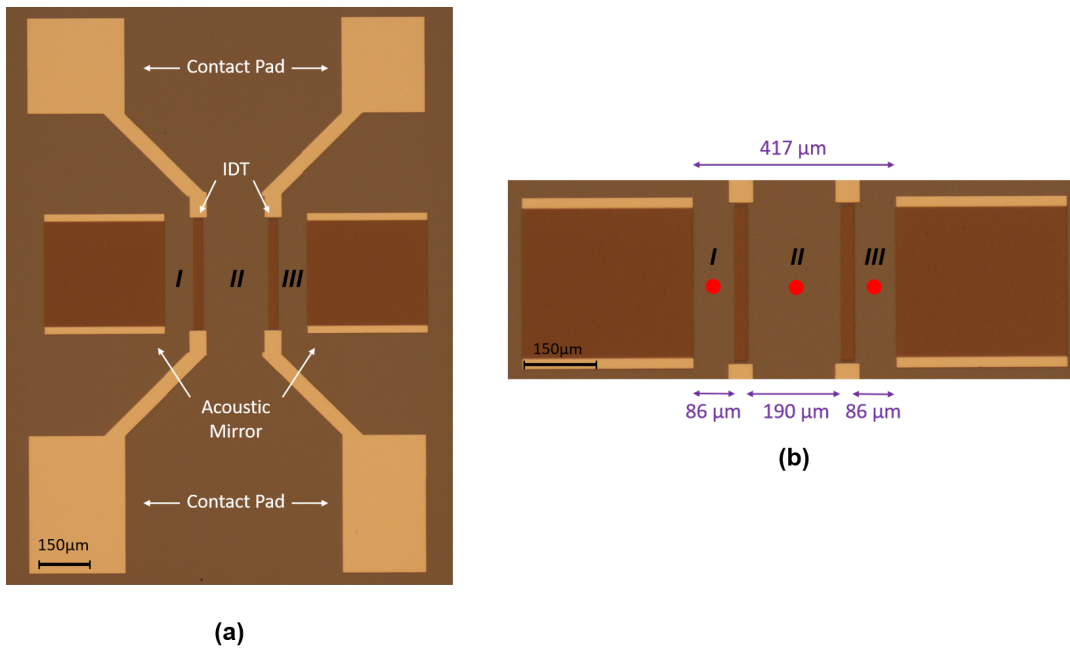
Figure 3.3: Sample A (a): This sample consists of two mirrors, both $N_m = 250$, and two IDTs, both $N_f = 10$. The mirror-mirror separation is roughly 417 µm. The distance between mirror-IDT, and IDT-IDT are depicted as well, as these structures form secondary resonators. The contact pads are wire bonded such that the IDTs can be driven by an RF generator. Three different regions on the sample are labeled *I*, *II*, and *III*. **(b)**: A zoomed-in picture of (a). The red dots indicate the locations of the laser beam at the time of recording the acoustic resonance spectra.

Figure 3.3 shows sample A after lift-off (see Sec. 4.1 for details about this step in the fabrication process). The device consists of a piece of GaAs patterned with two acoustic mirrors with 250 fingers each, and two IDTs with ten finger pairs (thus 20 fingers in total) each. All structures are made of 5 nm of titanium, 60 nm of aluminum, and covered with another 5 nm of titanium. The outermost-finger-to-finger distances are depicted in purple. The left IDT is excited with an RF generator.

3.4.1   Resonances

Sample A is designed to have a resonance frequency of roughly 1 GHz. The speed of surface waves on GaAs is approximately 2860 m/s. The corresponding wavelength for 1 GHz waves is $\lambda_{GaAs} \approx 2860 \text{ ms}^{-1}/(10^9 \text{ s}^{-1}) \approx 2.86$ µm. Hence, the center-to-center finger spacing of both the mirrors and the IDTs are designed to be 1.4 µm. Because the wave speed is slower underneath metal structures and the presence of imperfections in the design and substrate, the resonance frequency

will most likely not be precisely at the anticipated value. Therefore, it is essential to construct the acoustic resonance spectrum of an acoustic resonator prior to excitation and measurement of the displacement.

Three separate acoustic resonance spectra are obtained for sample A. An acoustic resonance spectrum is measured by focusing the laser beam somewhere on the sample and exciting the RF generator with a range of frequencies. The spectrum analyzer measures the spectrum of the PD signal, centered at the excitation frequency with a span of 10 kHz. The SAW signal will appear as a peak in this spectrum, and its amplitude corresponds to the peak value. Each graph in 3.4 corresponds to one of the red dots in Fig. 3.3.

(a)   (b)   (c)
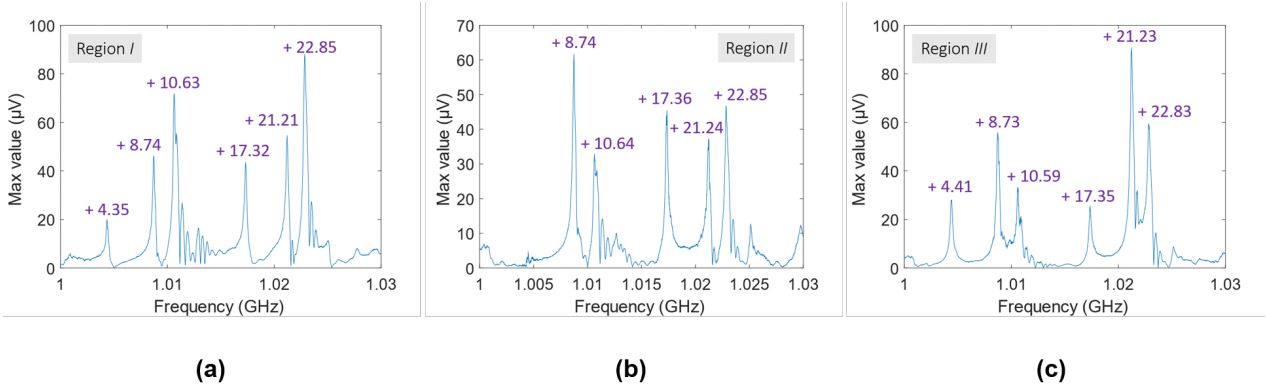
Figure 3.4: Acoustic resonance spectra of sample A The maximum response of the spectrum analyzer is plotted against the range of frequencies by which the left IDT is excited. The resolution is 10 kHz. All purple numbers correspond to peaks, the numbers are in MHz and should be added to 1 GHz. Figure 3.3 indicates the different regions on the sample. The red dots in the same figure mark the position of the focused laser beam at the time of the frequency sweeps. The same resonance peaks are present in all three regions, except for the first resonance peak in (b). The height of the resonance peaks is position dependent as the amplitude of standing waves is position dependent.

Figure 3.4 shows that among the different regions, resonance peaks are present at approximately the same frequency. However, the height of the peaks varies among the three measurements. The acoustic resonance spectrum is sensitive to the location of the focused laser beam. A resonance peak is greatest when the measurement is performed with the laser beam focused at the location of an anti-node for that specific frequency. Moreover, certain peaks within one spectrum possibly correspond to different sub-resonators. It is not straightforward to relate the peaks to a specific sub-resonator, as the coupling of the different sub-resonators influences the exact frequencies of the resonances. Two of the sub-resonators correspond to regions *I* and *III*. The length of these sub-resonators is 86 µm, so their effective length will be slightly larger, roughly 100 µm. According to Eq. 2.5, $\Delta f_{FSR} \approx 0.012$ GHz for this effective length. Peak separations of this size can be found in Fig. 3.4. The largest sub-resonator has a length of 190 µm. For an effective length of 200 µm, the free spectral range would be $\Delta f_{FSR} \approx 0.007$ GHz. Again, this peak separation can be found in the acoustic resonance spectra. However, there is no consistent pattern, probably due to the coupling of the different sub-systems. A system consisting of only one resonator would simplify the analysis of the acoustic resonance spectrum.

Based on the acoustic resonance spectra presented in Fig. 3.4, there are six frequencies that can be used to excite the IDT. In the remainder of this chapter, $f_0 = 1.02282$ GHz is used as resonance frequency.

3.4.2   Displacement maps

Sections of sample A are scanned with the Michelson interferometer, while the left IDT is excited with $f_0 = 1.02282$ GHz. The resulting displacement maps are shown in Fig. 3.5 (a). The maps distinctly shows standing waves. The SAW amplitude is not constant among the sub-resonators; the amplitude is greater when one of the confinements is a mirror. The left IDT is excited, and the amplitude to the left of this IDT is the greatest. The sub-resonators all couple to each other, complicating the analysis of the wave amplitude. Furthermore, the wavefronts seem to curve slightly away from the finger center. The wave pattern extends beyond the sections that are shown.
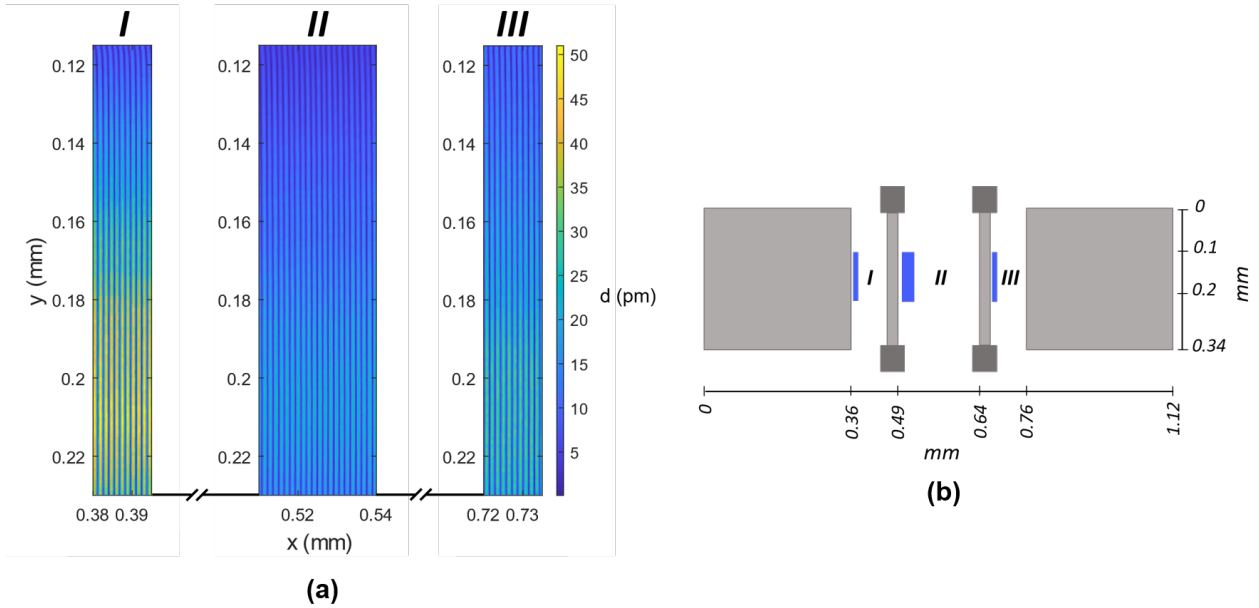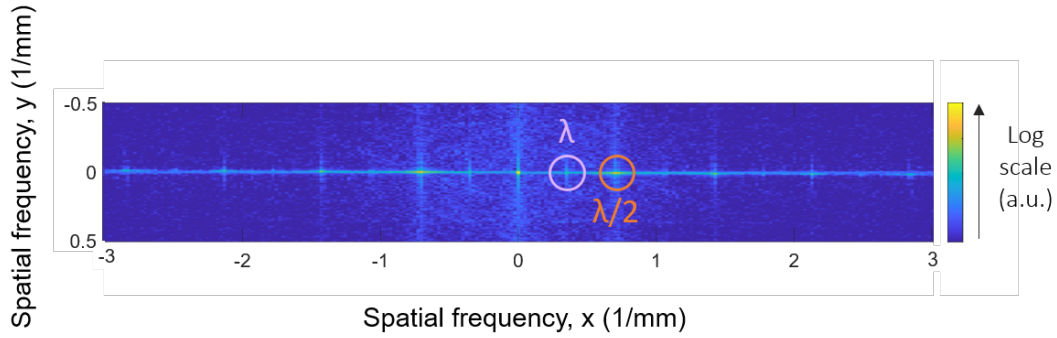

Figure 3.5: Displacement maps of sample A (a): Displacement maps of three sections of sample A. The locations of the sections (*I*, *II*, and *III*) are indicated by blue regions in **(b)**. The resolution in the x-direction is 100 nm and the resolution in the y-direction is 1 µm. The left IDT is excited with $f_0 = 1.02282$ GHz. The colorbar is applicable to all three segments. Clearly, a standing wave pattern is visible in all three sections. The amplitude of the standing waves varies among the sections and among the y-position within one section. **(b)**: A diagram of sample A based on Fig. 3.3.

The standing wave amplitude is not constant along the y-axis. In all three sections, the displacement is greatest around y = 0.21 mm and smoothly decays outwards. At heights where there is no acoustic mirror, there is no wave pattern (not shown). Figure 3.5 does not clearly show it, but the peak amplitude is not positioned at half the finger length, but slightly lower. Previous research [13] and [15] has shown that the amplitude profile corresponds to the zero-order transverse acoustic mode. Above the fundamental resonance frequency, higher order transverse modes have been observed.

The presence of standing waves can be verified by taking Fourier transforms of the displacement maps. Figure 3.6 depicts the fast Fourier transform of Fig. 3.5 (a) region *I*. A multitude of peaks are visible in this transform. The second strongest peak corresponds to $\lambda_{saw}/2 \approx 1.4$ µm and thus to the standing wave, as the spectrum analyzer records the time-averaged maximum displacement. The subsequent peaks (third and higher) are the higher harmonics of the $\lambda_{saw}/2$-signal, they result from the fact that the standing wave pattern is not sinusoidal, but exhibits sharp dips (see Fig. 3.7). The first peak in the spectrum corresponds to $\lambda_{saw} \approx 2.8$ µm. This periodicity is likely to stem from the BAWs that are generated by the IDT as a secondary effect.

Figure 3.7 shows slices along the x-axis of the data shown in Fig. 3.5 (a), region *I*. The wave

Figure 3.6: Fast Fourier transform of the displacement map of sample A, region *I* The FFT shows multiple peaks. Most notably, there is a peak corresponding to the wavelength of the excited SAWs ($\lambda_{saw} \approx 2.8$ µm) and a peak corresponding to half the wavelength ($\lambda_{saw}/2 \approx 1.4$ µm). The $\lambda_{saw}/2$-periodicity is the signal that is expected when SAWs with wavelength λ_{saw} are present, because the spectrum analyzer only records the time-averaged maximum displacement. The λ_{saw}-periodicity likely stems from the presence of BAWs. The peaks beyond $\lambda_{saw}/2$ are higher harmonics that account for the sharp minima in the standing wave pattern, see Fig. 3.7.
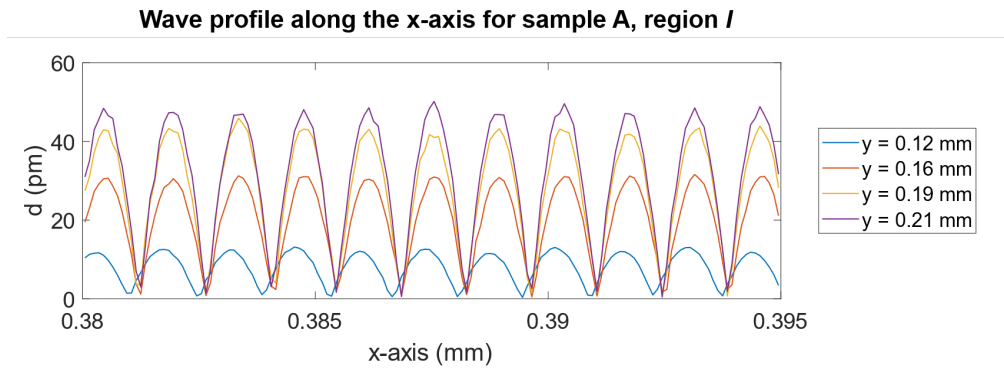
Figure 3.7: Wave profiles along the x-axis of sample A, region *I* For four different y-positions, a profile of the standing wave along the x-axis is shown. The profiles are extracted from the data presented in Fig. 3.5 (a) region *I*. The amplitude decreases when moving away from the central peak at y = 0.21 mm. The locations of the peaks for y = 0.12 mm are shifted compared to the other graphs, this agrees with the observation from the displacement maps (Fig. 3.5) that the wavefronts curve near the edges.

profiles show smooth maxima and sharper minima. The amplitude decays as the y-position moves away from the central peak at y = 0.21 mm. The $\lambda_{saw}/2$-periodicity is clearly visible, whereas the λ_{saw}-periodicity cannot be seen.

Design and Fabrication of Surface Acoustic Wave Resonators

In the previous chapter, 3, the scanning Michelson interferometer was introduced. The interferometer is used to obtain acoustic resonance spectra, and displacement maps of SAWs inside acoustic resonators. Sample A was introduced to set a baseline for these measurements. It was mentioned that sample A is not necessarily a good acoustic resonator. The requirements for being a "good" resonator depend on the context. This chapter will detail the requirements of a good resonator within the context of this thesis. The design considerations to fulfill these requirements, such as configuration, choice of metal, and metal thickness, will be discussed. To ensure an effective discussion of the device requirements and design considerations, this chapter starts with a detailed account of the fabrication process of acoustic resonators.

4.1   Fabrication

During this thesis, all SAW resonators were fabricated on gallium arsenide (GaAs) in (001)-cut and in [110]-direction. As required for the functioning of IDTs, this substrate is a piezoelectric material. The electromechanical coupling coefficient of GaAs is relatively low: 0.07% [3]. On one hand, high coupling leads to higher efficiency from input voltage on the RF generator to subtrate displacement. On the other hand, certain loss mechanisms scale with the electromechanical coupling, making lower coupling desirable. For the purpose of this research, high efficacy is not a requirement, making GaAs an appropriate choice. Moreover, SAWs can be coupled to quantum dots. The quatum dots available to this research are InGaAs embedded in GaAs, providing another reason for working with GaAs.

Electron-beam (e-beam) lithography is a widely used technique in nanofabrication. It allows for writing custom patterns on a substrate, which can be filled with some material (for instance a metal) later on. E-beam lithography is especially useful for the creation of GHz SAW resonators. In Sec. 2.1 it was discussed that the finger spacing is dominated by the SAW speed and the desired frequency: $d = \lambda_{saw}/2 = v_{saw}/2f_0 \approx 1.4$ µm. For a metallization rate of 50%, the finger width will be smaller than a micrometer. This structure size is attainable with e-beam lithography.

Figure 4.1 shows the fabrication process of the samples presented in this thesis. The first step is cleaning the GaAs substrate. Substrates are first placed in acetone and then in isopropanol. Samples that are especially dirty, are placed in an ultrasonic bath for roughly five to ten minutes. After this cleaning process, the substrate is dried with nitrogen gas.

Next, the positive e-beam resist PMMA (polymethyl methacrylate) is spin coated on top of the GaAs. Two different layers of PMMA are deposited: first a layer of 600K PMMA (4000 rpm), then a layer of 950K PMMA (4000 rpm). After each layer, the substrate is baked for 2 minutes at 180°C, to harden the PMMA. PMMA is a polymer consisting of long chains. When PMMA comes into

contact with an e-beam, the polymer chains will be broken down. 600K PMMA breaks down more easily compared to 950K PMMA. Once the spin coating is completed, the sample is patterned by the e-beam according to a design file. Because 600K PMMA reacts more strongly to the e-beam, exposure will lead to an undercut in the PMMA layers. This undercut is not shown in Fig. 4.1.

After patterning, the sample is placed into some developing-agent (1:3 MIBK/IPA). The polymer chains that have been broken down by the e-beam, dissolve in this liquid, leaving the bare substrate behind. The unpatterned sections of PMMA will remain intact.

The next step is the metal evaporation. The sample is placed upside-down in an e-beam evaporator. In this machine, a high vacuum is created and a crucible filled with a metal (aluminum for this thesis) is struck by an e-beam, causing metal to evaporate. The evaporated metal will deposit on the upside-down sample, that is placed directly above the crucible. The metal thickness can be regulated with an accuracy of at least a few nanometers.

The evaporation covers the entire substrate in metal. The unwanted sections of metal are removed during the lift-off. For this step, the sample is immersed in acetone for some time ranging from a couple of hours, up to a day. The acetone dissolves all remaining PMMA, lifting the metal that is on top. The lift-off time depends on the choice of metal and type of structures that are patterned. The undercut caused by the two different PMMA layers assists in the lift-off. This undercut will restrict the amount of metal that can be evaporated onto the bare substrate. That means that after the metal evaporation, there will be small parts of substrate in between the GaAs-Al and GaAs-PMMA-Al sections, that are covered with neither PMMA nor Al. On these small parts of substrate, acetone can penetrate, thereby facilitating the lift-off.

Finally, the sample is wirebonded: the IDT contact pads are connected to SMA connectors. This allows for driving the IDT with a RF generator.
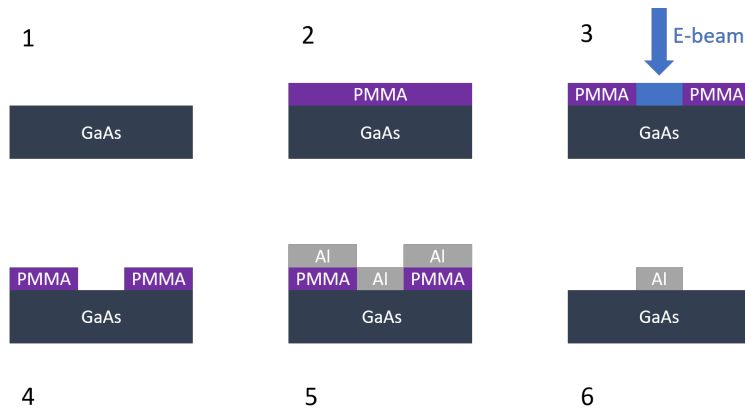
Figure 4.1: Electron-beam lithography and metal evaporation For this thesis, SAW resonators are fabricated with electron-beam (e-beam) lithography. **(1)**: A piece of GaAs is cleaned with acetone and isopropanol. **(2)**: PMMA (positive resist) is spin coated on top of the GaAs. **(3)**: An e-beam patterns the sample according to a design file. **(4)**: The sample is put into a developing-agent that dissolves all PMMA that has been exposed to the e-beam. **(5)**: A thin (5-100 nm), even layer of aluminum (Al) is evaporated on top of the sample. **(6)**: During the lift-off process, the sample is immersed in acetone. All remaining PMMA (and metal that has been deposited on top) will be removed.

4.2   Design considerations

The design of an acoustic resonator depends on the requirements of the application. In this thesis, the objective is to image standing SAWs inside an acoustic resonator with a scanning Michelson interferometer and to investigate the effect of different metal thickness on the finesse of the resonator. The prospective goal of the project is to image thermal SAWs inside an acoustic resonator with an open microcavity. Considering these applications, the following design requirements can be formulated:

1. The acoustic resonator should contain one IDT to electrically excite SAWs (not required when performing thermal phonon measurements with an open microcavity).

2. The effect of sub-resonators should be minimized to simplify the analysis of the acoustic resonance spectra.

3. The mirror bandwidth should fall within the IDT bandwidth.

4. The resonator area should be large enough to allow for optical probing.

5. The resonator area should be minimized (as much as allowed by the previous requirement) to enhance SAW displacement.

6. The resonator finesse should be maximized to enhance SAW displacement.

The impact of requirements 1-5 on the design of the resonators will be touched upon in Sec. 4.2.1. The impact of the 6th requirement is the focus of Sec. 4.2.2. Whereas this chapter follows a more theoretical approach, chapter 5 covers measurement results. These results concern requirement 6 as they demonstrate the influence of the metal thickness on the resonator finesse.

4.2.1 Configuration

Requirements 1-5 dictate the configuration of the acoustic resonator. By configuration, the number of fingers pairs in the IDT (N_f), the number of fingers in the mirror (N_m), the placement of the IDT with respect to the mirrors, and the mirror separation is meant. As stated by the first requirement, the design will include one IDT.

Recall from Secs. 2.2 and 3.4.1 that as a secondary effect, IDTs reflect SAWs. Placing an IDT somewhere between the two acoustic mirrors (as was done for sample A, Sec. 3.4), will therefore lead to the creation of sub-resonators. To avoid any unnecessary complications, the effect of sub-resonators should be minimized. This can be done by placing the IDT next to the mirror, with a separation of $d = \lambda_{saw}/2$ between the outermost edges of the mirror and IDT. In this case, the IDT will simultaneously function as a SAW transducer and as an extension of the mirror. This will not completely nullify the effect of sub-resonators, as both an acoustic mirror and IDT (when functioning as a mirror) are associated with a penetration depth. However, the effect will be minimized, thereby satisfying requirement 2.

In practice, it proves to be challenging to pattern an IDT directly next to a mirror because of the proximity effect. During the e-beam patterning, the electrons scatter both in the resist layer and substrate, thereby enlarging the area exposed to electrons (with respect to the area defined by the design file). Moreover, the scattered electrons create secondary electrons that amplify this effect even more. Figure 4.2 shows three different designs in which the IDT is placed adjacent to the mirror, with a separation of $d = \lambda_{saw}/2$. Every colored (pink or orange) area in the design file is patterned by the e-beam. In other words, all colored areas receive a certain dosage of electrons. The dosage can be specified in the e-beam lithography software. A dosage of 1.0 indicates the standard setting, whereas a dosage of 0.8 indicates 80% of the standard setting. The standard depends on the PMMA recipe and e-beam settings. Lowering the dosage decreases the proximity effect and thus the enlargement of the patterned sections with respect to the design file. However, when the dosage is too low, not all sections of PMMA as indicated by the design can be removed during the developing step.

From Fig. 4.2 it can be concluded that a lower dosage is effective in diminishing the proximity effect and allowing for the placement of an IDT directly next to a mirror. The dosage can be lowered either through eliminating the overlap between fingers and busbars, adjusting the design such that large areas (busbars) are separated as much as possible, or lowering the dosage setting in the e-beam. Design (c.i) proves to be successful, however, it is not used for the results presented in chapter 5.
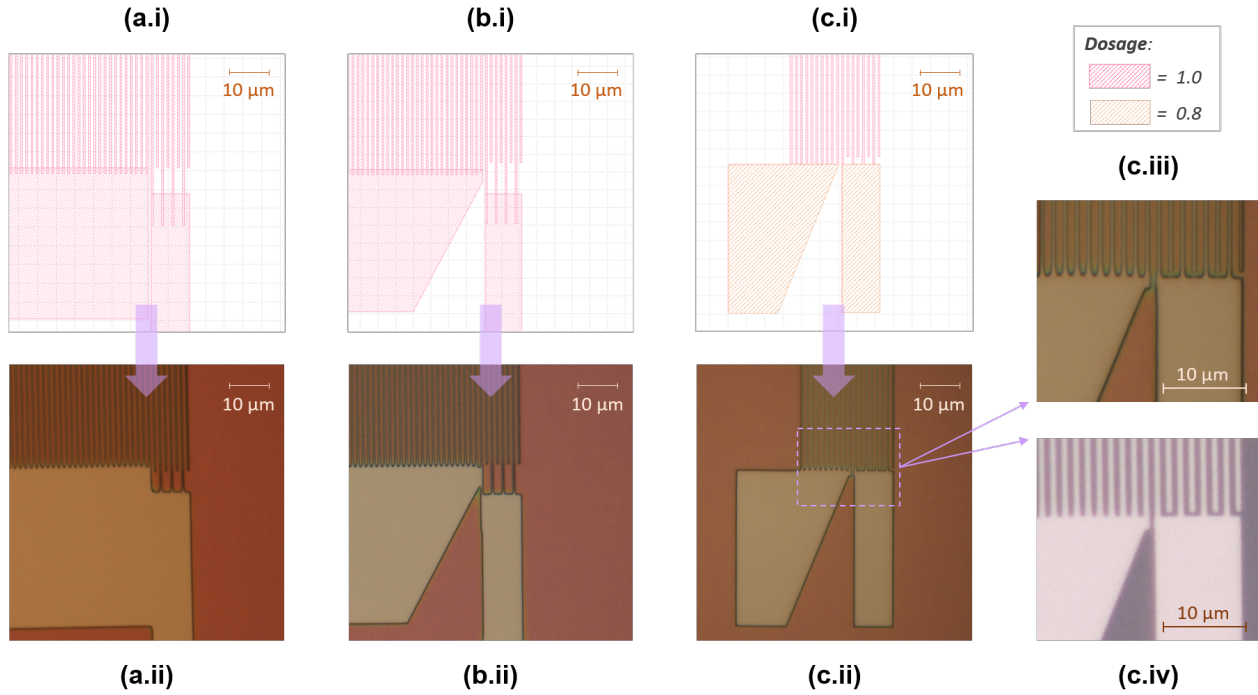
Figure 4.2: Different design options and the proximity effect. (a.i): Design file in which the IDT is placed next to the mirror (with a separation of $d = \lambda_{saw}/2$) without any modifications. **(a.ii)**: The sample after developing. Pink/orange sections are PMMA, yellow/brown sections are bare GaAs. Because of the proximity effect, the outer-left IDT finger, the mirror busbar, and IDT busbar have become connected. **(b.i)**: Design file in which the IDT is placed next to the mirror, but the busbar of the mirror is slanted. The overlap between the outermost finger of the mirror and mirror-busbar is decreased. **(b.ii)**: The sample after developing. The outer-left finger of the IDT still has merged with the busbar of the mirror, although to a lesser degree compared to (a.ii). **(c.i)**: Design file in which there is no overlap between fingers and busbar for both the IDT and mirror. Also, the dosage of the busbars is lowered to 0.8. **(c.ii)** and **(c.iii)**: The sample after developing. All structures are separated. **(c.iv)**: The sample after metal evaporation and lift-off. Also after depositing metal, the structures are well separated. See List of Samples (A) for more information on these three samples.

Requirement 3 states that the mirror bandwidth should fall within the IDT bandwidth. When this is not the case, the standing waves that are excited by the IDT cannot be reflected by the mirrors and no standing wave pattern will emerge. The spacing of both the IDT and mirror fingers is $d = \lambda_{saw}/2$. Therefore, the bandwidth for both structures will be centered roughly around 1 GHz. The bandwidth of the IDT is dictated by Eq. 2.2 from Sec. 2.1. For an IDT with $N_f = 10$, the 3 dB bandwidth is $\Delta f = 90$ MHz. In the acoustic resonance spectra of sample A (Fig. 3.4) multiple peaks are visible. Therefore, it can be concluded that for acoustic mirrors with $N_m = 250$ and IDTs with $N_f = 10$, the mirror bandwidth is contained within the IDT bandwidth.

To meet requirements 4 and 5, the acoustic aperture (IDT finger length) and mirror separation should be addressed. As mentioned in Sec. 2.1, the acoustic aperture should be much larger than the SAW wavelength to limit diffraction: $W > 100\lambda_{saw}$. For the samples presented in this thesis, an aperture of roughly 300 µm is chosen, such that: $W \approx 107\lambda_{saw}$. The mirror-to-mirror separation could be as small as 10 µm, since the beam waist of the focused laser beam in the interferometer setup is roughly 1.2 µm. This would leave enough space for optical probing. However, for the samples presented in chapter 5, the separation is roughly 400 µm. This is because of some technicalities of the e-beam lithography step: the design is subdivided into write fields. Sections of design that overlap multiple write fields tend to be slightly misaligned in the final patterning. The writefields during this project were set to 400 µm by 400 µm. For the current design, both mirrors roughly fill one writefield. This makes it convenient to leave one writefield of unpatterned space in between the

mirrors. Changing the settings of the e-beam and improving the writefield alignment would allow for smaller resonator volumes. After all, the thermal phonon displacement increases by a lot for a separation of 10 μm compared to 400 μm.

4.2.2   Choice of metal and metal thickness

The last requirement is a high finesse. In theory, the resonator finesse only depends on the reflectivity of the mirrors (see Eq. 2.7 in Sec. 2.2). However, this equation does not account for propagation loss of the SAWs in between the mirrors and scattering into BAWs by the mirrors. A derivation of the finesse that takes into account both loss through propagation, as well as loss associated with reflection by the mirrors, is provided in [24].

To achieve high mirror reflectivity, the mirror-array should contain a sufficient number of fingers. In Sec. 3.4 it was found that sample A, an acoustic resonator with two mirrors with $N_m = 250$ each, exhibited resonance peaks and standing waves. This number of fingers is therefore believed to be sufficient.

Additionally, the acoustic mirror reflectivity can be tuned through the choice of metal and metal thickness. 'Thickness' in this context means the height of the metal out of the substrate plane. In Sec. 2.2 it is discussed that reflection by an acoustic mirror happens through two mechanisms: electrical and mechanical impedance mismatch. The mechanical contribution to the reflection is dominant. The mechanical impedance mismatch arises because of mass loading: the weight of a metallic finger onto the substrate slightly changes the wave velocity underneath the finger. This difference in wave velocity that the SAW experiences when it encounters a finger, causes partial reflection of the SAW. The degree of mass loading is proportional to the mass and thus the metal thickness and metal density.

In previous research, different metal compositions on GaAs have been tested. Aluminum is a common choice, despite the fact that it will not always perfectly stick to GaAs. Therefore, a thin layer of for example titanium can be deposited first. A composition of Ti/Al, 5/30 nm has been tested in [21]. To prevent oxidation of the aluminum, another layer of titanium can be deposited on top of the aluminum layer, for example with thicknesses Ti/Al/Ti, 10/30/10 nm in [17] and [14]. The composition 5/60/5 nm for these metals has been tried in [21]. In [25], only a 50 nm layer of aluminum has been used, without a sticking- or anti-oxidation layer. Besides aluminum, gold with a sticking layer of chromium has also been used in compositions 5/30 nm, 5/50 nm, and 5/60 nm, see [21].

All samples presented in this thesis were fabricated with aluminum instead of gold. Although both metals have a relatively low electrical resistivity, the mass density is rather different ($\rho_{Al} = 2.70\,\text{g/cm}^3$ and $\rho_{Au} = 19.3\,\text{g/cm}^3$). Because of gold's high mass density, the mass loading increases relatively quickly with thickness. From earlier research, it seems that a thickness between 30 and 60 nm is reasonable. The mass loading and thus reflectivity in this range are better tunable for aluminum mirrors compared to gold mirrors.

As mentioned in Sec. 4.1, the lift-off time depends on the choice of metal and the type of structures that are patterned. During this research, it was found that sections of metal on PMMA that are smaller than a micron and that are surrounded by metal on bare GaAs, can be challenging to remove during lift-off. The sections in between mirror fingers for a GHz resonator fall under this category. The lift-off of the GHz mirrors when gold is used, proved to be more problematic than when aluminum is used. This fabrication issue is yet another reason to favor aluminum over gold.

4.2.3   Other considerations

There are other design choices that can further enhance the performance of acoustic resonators in general. First of all, using curved reflectors limits loss. In Fabry-Pérot cavities, spherical mirrors that match the spatial light field are used to compensate for beam divergence. In acoustics, the same has been done in [17] and [14]. Using curved structures as opposed to straight structures complicates the fabrication process and is therefore not applied in this thesis. Moreover, the IDTs and mirrors are expected to function more efficiently when the associated resistance is low. A smaller resistance leads to less dissipation of electrical energy and therefore a higher conversion into SAWs. It was found in [21] that the resistance of an IDT depends on both the finger area and busbar area.

Chapter 5

Finesse and Metal Thickness

One of the requirements from Sec. 4.2 was maximizing the resonator finesse to enhance displacement. It was stated that one of the mechanisms through which the finesse can be enhanced, is finding the optimal thickness of the acoustic mirrors. Increasing the thickness, increases the mass loading underneath the fingers. This mass loading is the basis of the primary reflection mechanism. However, it seems likely that increasing the thickness also increases the losses associated with scattering into BAWs by the mirror fingers [21]. For this reason, it is interesting to find the optimal thickness of aluminum on GaAs.

In this chapter, three samples (B35, B50, and B100) that are identical in design apart from their metal thickness, will be introduced first. Then, for all three samples two types of measurement results (obtained by the Michelson interferometer) will be presented: the acoustic resonance spectra, and the displacement maps. From the resonance spectra, the effective cavity length L_{eff} and the finesse $\mathcal{F}$ will be calculated. From the displacement maps, the displacement field decay underneath the acoustic mirrors will be extracted. Lastly, a statement about the effect of the metal thickness on the mirror reflectivity and finesse will be made.
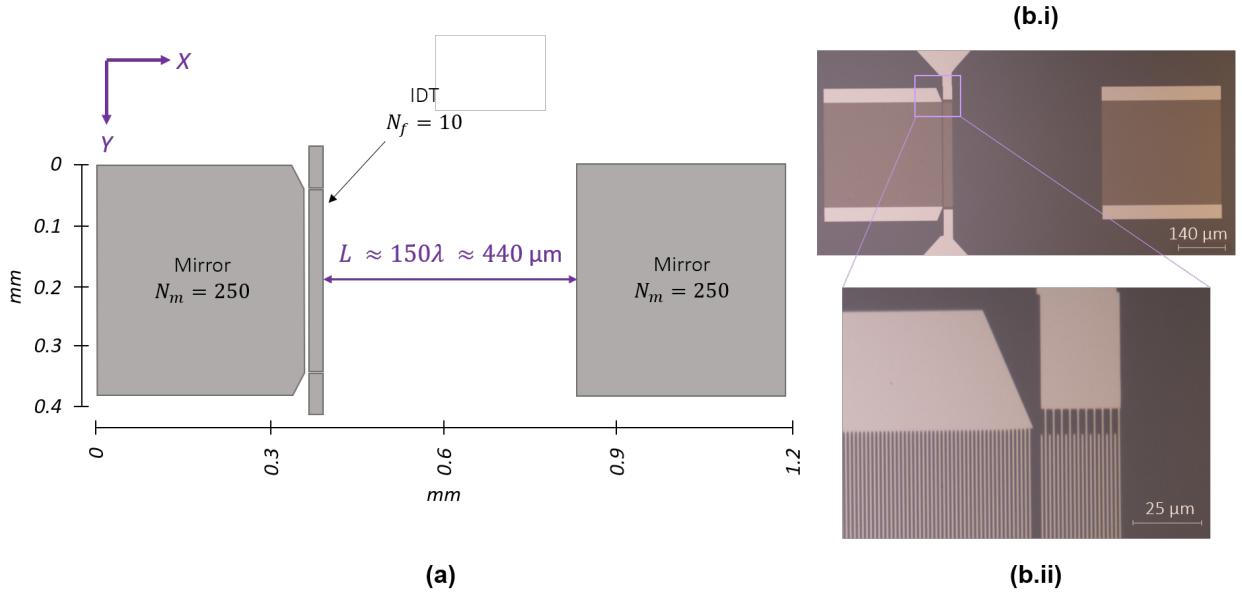
5.1 Sample design

The samples B35, B50, and B100 all look like the one presented in Fig. 5.1. The devices consist of two acoustic mirrors with $N_m = 250$ and an IDT with $N_f = 10$ that is placed close to the left mirror. The separation between the left mirror and IDT is approximately 3.5 µm. The upper comb of the IDT is connected to an RF generator, whilst the lower comb is grounded. The separation between the IDT and right mirror is roughly $150\lambda_{saw}$. All samples are made of aluminum on a GaAs substrate. The aluminum thickness is the only variable among the three samples. B35 has an aluminum thickness of 35 nm, B50 has an aluminum thickness of 50 nm, and B100 has an aluminum thickness of 100 nm.

As mentioned in Sec. 4.2.1, to optimize the SAW displacement and still allow for optical probing, the mirror separation could have been smaller. However, because of settings in the fabrication process, the mirror separation is not minimized for these samples.

5.2 Measurement results: Acoustic resonance spectra

Recall from Sec. 3.4.1 that the Michelson interferometer can be used to obtain acoustic resonance spectra. Such spectra show peaks corresponding to the resonance frequencies of the acoustic resonator. A measurement of this kind is performed by focusing the laser beam at a fixed position

Figure 5.1: The design of samples B35, B50, and B100. (a): Schematic of the sample configuration. **(b.i)**: Optical microscope image of sample B35. No images of B50 and B100 are shown because they look the same, as only the aluminum thickness is varied. **(b.ii)**: Zoomed in from (b.i).

inside the resonator. Then, the IDT is excited by a frequency-swept RF generator. For every frequency, the response of the RF photodiode and spectrum analyzer is recorded. From the locations of the peaks, the free spectral range (FSR) and thus the effective resonator length can be derived. The full width half max (FWHM) can be extracted as well, allowing for a computation of the finesse.

Two notes need to be made before presenting the results. First of all, for sample B50, the acoustic resonance spectrum is obtained with a VNA instead of the Michelson interferometer. There is no particular reason for this. Also for a VNA measurement, a sweep of frequencies is applied to the IDT. The S_{11} parameter gives the reflected power. When the IDT is excited at resonance, the reflected power – and thus the S_{11} parameter – will be low. The reflected power is low because the power is converted into standing waves. More details on VNA measurements on IDTs can be found in [21].

Secondly, to obtain a complete acoustic resonance spectrum with the Michelson interferometer, multiple spectra at different x-positions need to be measured and combined. When the spectrum is measured only at a single position, there is a likelihood that for one or more resonance frequencies, the position of the laser beam is at a node. When this is the case, that resonance frequency will not show as a peak in the spectrum. When combining spectra that are taken at different positions, the full response can be obtained. In Fig. 5.2 (a) and (c), only one of the fourteen spectra that were obtained in total, are shown. When performing a VNA measurement, only one measurement needs to be taken.

Based on the acoustic resonance spectra, the following values for the FSR and effective cavity length are found:

$$\Delta f_{FSR,B35} = 2.52 \pm 0.10 \,\text{MHz}, \ L_{eff,B35} \approx 567 \,\text{µm}$$
$$\Delta f_{FSR,B50} = 2.58 \pm 0.12 \,\text{MHz}, \ L_{eff,B50} \approx 554 \,\text{µm} \tag{5.1}$$
$$\Delta f_{FSR,B100} = 2.73 \pm 0.10 \,\text{MHz}, \ L_{eff,B100} \approx 524 \,\text{µm}$$

The FSR increases with metal thickness. Consequently, the effective length decreases with metal thickness.
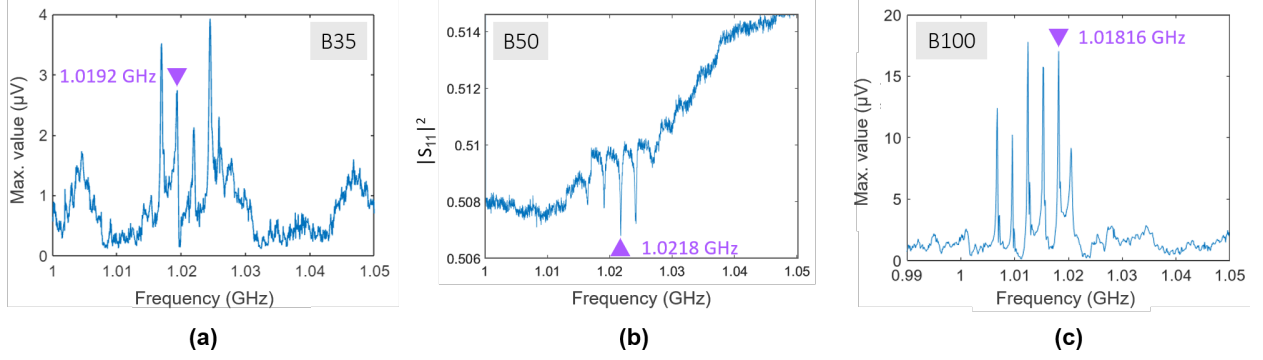
Figure 5.2: Acoustic resonance spectra of samples B35, B50, and B100. The purple triangles indicate the excitation frequency f_0 when obtaining displacement maps, see Sec. 5.3. **(a)**: Acoustic resonance spectrum of sample B35, obtained with the Michelson interferometer, taken at position $x = 749.4$ µm. **(b)**: Acoustic resonance spectrum of sample B50, obtained with a VNA. **(c)**: Acoustic resonance spectrum of sample B100, obtained with the Michelson interferometer, taken at position $x = 631.2$ µm.

In Sec. 2.2 it was discussed that the finesse can be obtained either through the FSR and FWHM, or through the mirror reflectivity r_m. In the latter case, the system is considered to be lossless:

$$\mathcal{F} = \frac{\Delta f_{FSR}}{\Delta f_{FWHM}} \quad \mathcal{F}_{lossless} = \frac{\pi \sqrt{|r_m|}}{1 - |r_m|} \tag{5.2}$$

The FSR and FWHM can be extracted directly from the resonance spectra. The mirror reflectivity r_m on the other hand, is derived from the FSR under the assumption that there is no loss. The derivation can be found in [12, Ch. 2]. The mirror reflectivity r_m, follows from the single finger reflectivity r_e:

$$|r_e| = \frac{\frac{v_{saw}}{2f_0}}{L_{eff} - L} \quad \rightarrow \quad r_m = \tanh(N_m |r_e|) \tag{5.3}$$

The following values for the finesse are found:

$$
\begin{aligned}
\mathcal{F}_{B35} &\approx 6 & \mathcal{F}_{lossless,B35} &\approx 120 \\
\mathcal{F}_{B50} &\approx 10 & \mathcal{F}_{lossless,B50} &\approx 390 \\
\mathcal{F}_{B100} &\approx 11 & \mathcal{F}_{lossless,B100} &\approx 1570
\end{aligned}
\tag{5.4}
$$

The values for the finesse based on the FSR and FWHM, $\mathcal{F}$, are considerably smaller than the values based on the mirror reflectivity $\mathcal{F}_{lossless}$. The latter values for the finesse are not reliable as the assumption that there is no loss, is wrong. Firstly, there are losses associated with propagation of the waves. Both beam divergence and dissipation by the substrate contribute to the propagation loss. Secondly, there is loss associated with the mirror fingers. Depending on the degree of mass loading, a portion of the SAWs will be scattered into BAWs by the electrodes. Therefore, the former values for the finesse $\mathcal{F}$ accurately represent the resonator quality.

There is an increase in finesse from 6 to 10 as the metal thickness increases from 35 nm to 50 nm of aluminum. The increase in finesse from 50 nm to 100 nm is significantly smaller. A possible explanation is that an increase from 35 nm to 50 nm causes an increase in reflectivity that is greater than the increase in mirror-associated loss (scattering into BAWs), such that the finesse increases. On the other hand, the increase in mirror-associated loss might almost fully compensate the increase in reflectivity for the step from 50 nm to 100 nm. When these two effects are in balance, there is no change in the finesse.

Another explanation is that the propagation loss limits a significant increase in finesse beyond a thickness of 50 nm. The total propagation loss depends on the propagation loss per round-trip and the total number of round trips that a SAW can make before being completely diminished by loss. As the reflectivity increases, the number of round-trips increases as well. Therefore it is possible

that beyond an aluminum thickness of approximately 50 nm, the propagation loss limits an increase in finesse, despite an increase in reflectivity.

5.3   Measurement results: Displacement maps

The Michelson interferometer is also used to obtain displacement maps, see Sec. 3.4.2. The IDT is excited by a fixed frequency f_0 that corresponds to one of the resonances. Then, the focused laser beam is scanned over the sample to record the displacement from point to point. The displacement maps for all three samples are depicted in Figs. 5.3, 5.4, and 5.5.
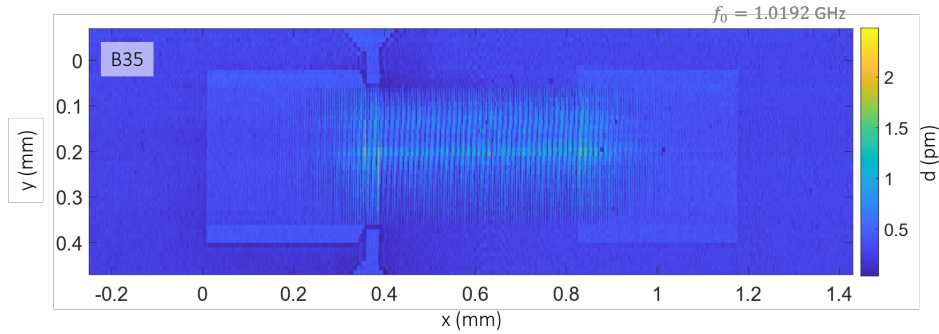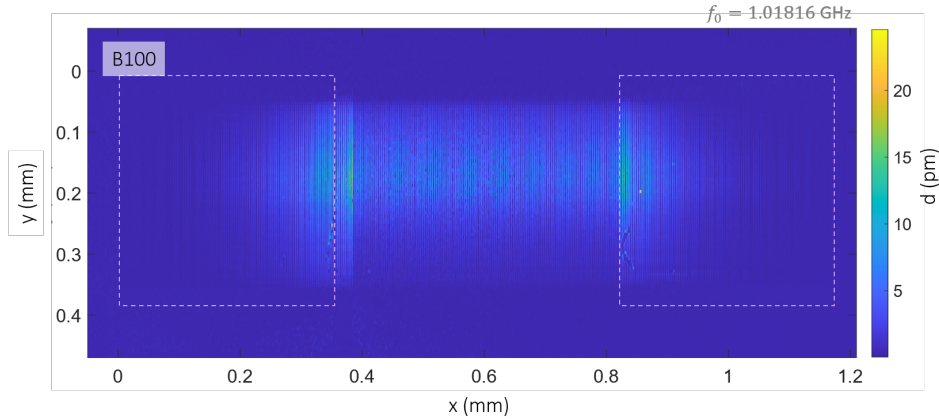

Figure 5.3: Displacement map of sample B35. The IDT is excited with $f_0 = 1.0192$ GHz. The map clearly shows the metal structures (mirrors, IDT, and parts of the contact pads). Also, there is displacement visible inside the resonator. This displacement decays with the penetration depth into the mirrors.
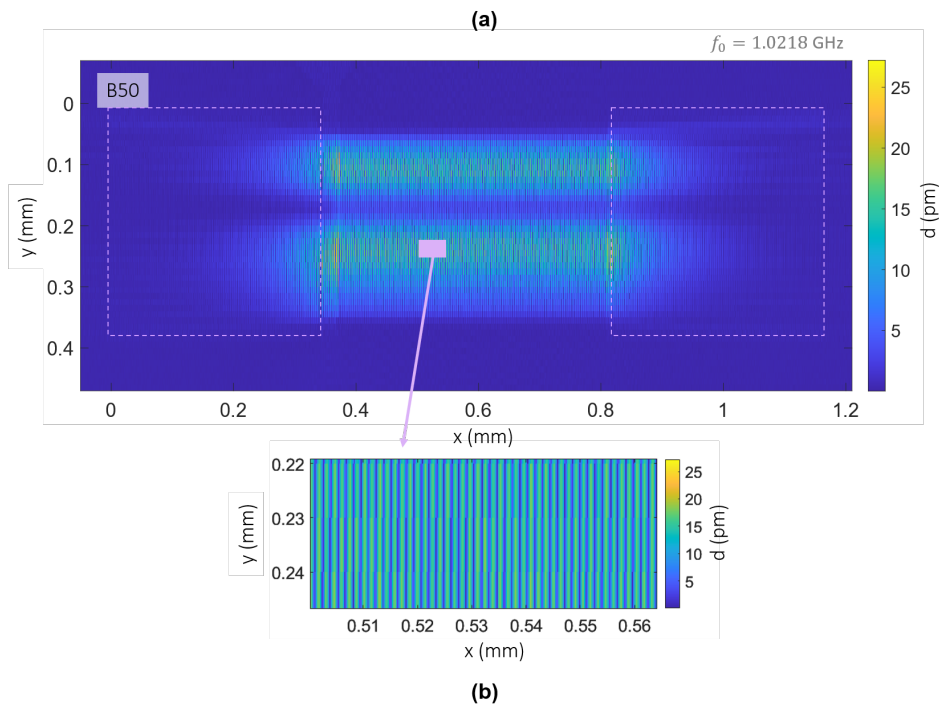
Figure 5.4: Displacement map of sample B50. The IDT is excited with $f_0 = 1.0218$ GHz. **(a)**: The metal features cannot be distinguished from the GaAs. Therefore, dashed boxed are drawn to indicate the approximate locations of the mirrors. There are two maxima present along the x-axis. This pattern resembles a transverse mode. Moreover, the displacement decays with the penetration depth into the mirrors. **(b)**: Zoomed in section of (a). The displacement clearly follows a standing wave profile.

All three maps show that there is displacement inside the resonator. Figure 5.4 (b) reveals that this displacement corresponds to a standing wave profile. Although not shown, the displacement in

Figure 5.5: Displacement map of sample B100. The IDT is excited with $f_0 = 1.01816$ GHz. The metal features cannot be distinguished from the GaAs. Therefore, dashed boxed are drawn to indicate the approximate locations of the mirrors. There is displacement visible inside the resonator, which decays with the penetration depth into the mirrors.

the maps corresponding to B35 and B100 also follows this profile. Hereby, the resonators are proved to sustain standing SAWs.

Figure 5.4 shows a displacement pattern that deviates from the patterns visible in figures 5.3 and 5.5. In Figs. 5.3 and 5.5, there is one maximum along the x-axis, whereas in Fig. 5.4 there are two maxima. This very much resembles the presence of a higher-order transverse modes. A similar but more extensive observation of this effect is discussed in [13] and [15]. The emergence of this seemingly transverse mode is not further investigated in this thesis, but this observation is not surprising as plane-mirror Fabry-Pérot resonators are unstable.

Note that in Figs. 5.4 and 5.5 the metal structures are not visible. The displacement in these figures is an order of magnitude larger compared to the displacement in Fig. 5.3. One could think that the displacement of samples B50 and B100 exceeds the displacement of B35 because of more effective wave generation by the IDT or better mirrors. However, the difference in displacement magnitude can also be caused by the difference in impedance matching between IDT and RF generator.
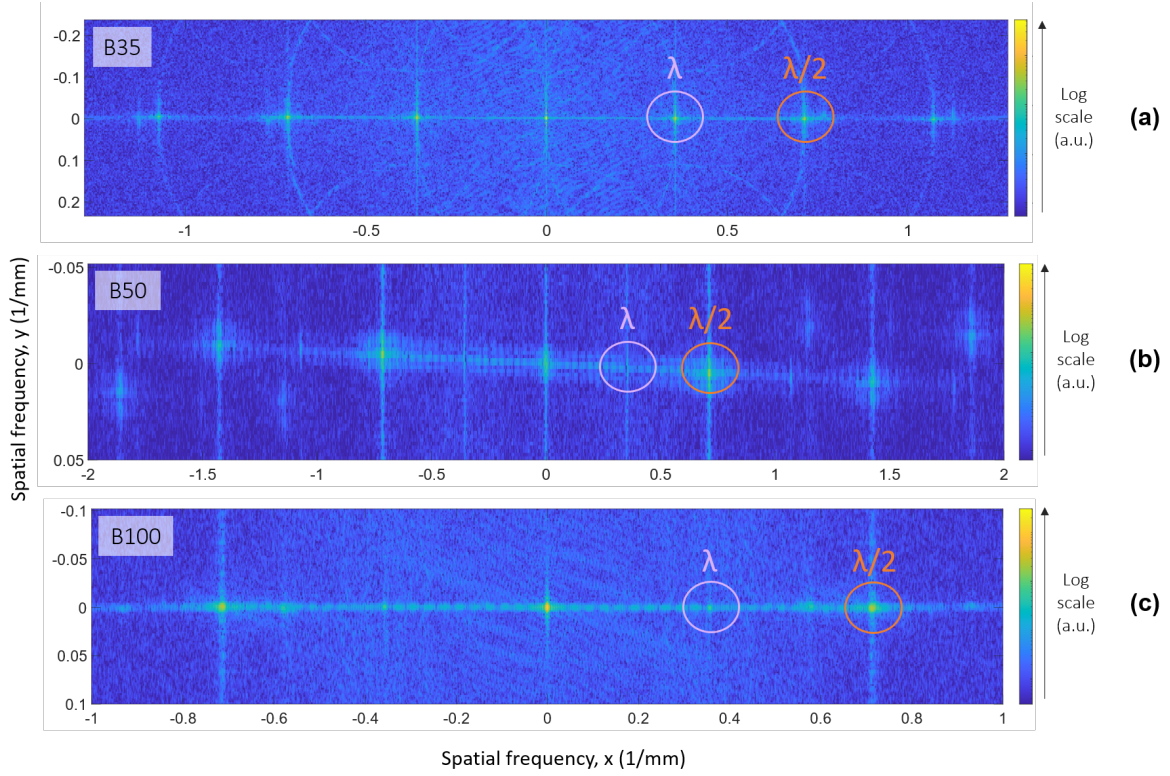
5.3.1 Fourier Transforms

Figure 5.4 (b) already illustrated that standing waves form inside the resonators. To further investigate these standing waves, fast Fourier transforms of the displacement maps are performed. Figure 5.6 shows the results for all three samples.

In all three Fourier transforms, a peak corresponding to a $\lambda_{saw}/2$-periodicity is present. These peaks confirm that in all three samples, standing waves with wavelength λ_{saw} are excited (see Sec. 3.4.2). Additionally, the higher harmonics of the $\lambda_{saw}/2$-periodicity, and the λ_{saw}-periodicity are visible. The latter likely stems from BAWs but this will not be further investigated in this thesis.

Besides the peaks, the transforms show other features. First of all, a line at spatial frequency y = 0 is visible for all three samples (although slanted for B50). This is an artefact of the fast Fourier transform and has no further significance. The vertical lines emerging from the peaks have the same origin. Furthermore, Fig. 5.6 (a) shows circle-like patterns that are likely to stem from diffraction effects. Lastly, the transform of B50 seems to be slanted. This is because of imperfect alignment of the XY-translation unit with respect to the SAW device.

Figure 5.6: Fast Fourier transforms of the displacements maps (a): FFT of the displacement map in Fig. 5.3, corresponding to sample B35. **(b):** FFT of the displacement map in Fig. 5.4, corresponding to sample B50. **(c):** FFT of the displacement map in Fig. 5.5, corresponding to sample B100. In all three transforms, peaks corresponding to the λ_{saw}-periodicity and the $\lambda_{saw}/2$-periodicity are visible. The $\lambda_{saw}/2$-periodicity is direct evidence of the presence of standing waves with wavelength λ_{saw}. Higher harmonics of this periodicity are visible as well. The λ_{saw}-periodicity is likely caused by the presence of bulk waves.
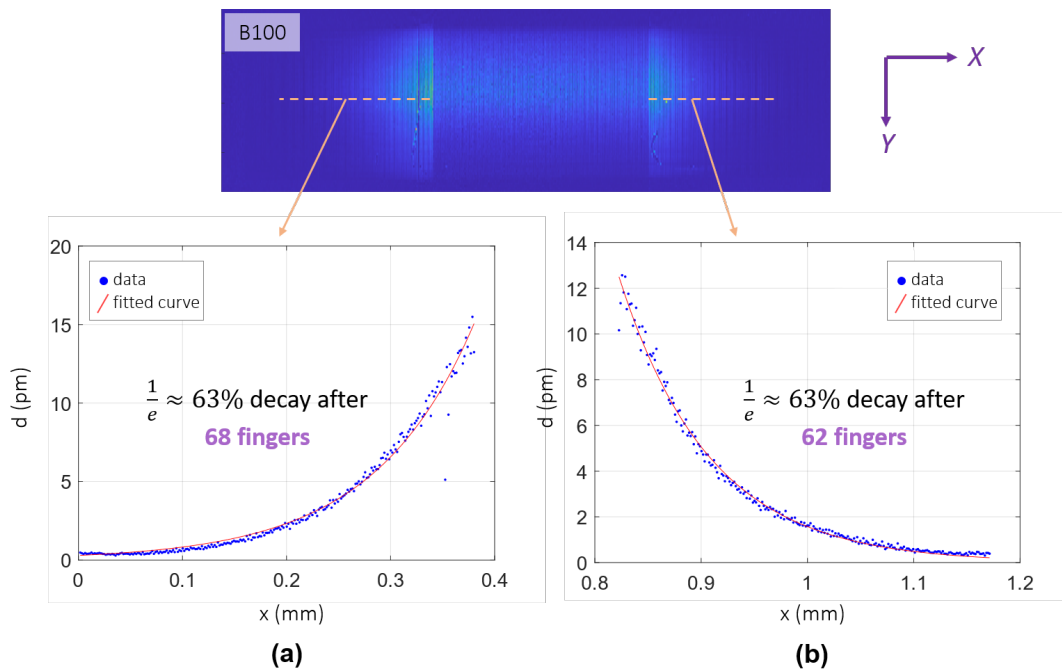
5.3.2 Exponential decay

In Sec. 5.2, the acoustic resonance spectra of B35, B50, and B100 are analyzed. From the data, values for the finesse are extracted, see Eq. 5.4. The finesse is a measure of the quality of the resonator. The displacement maps can also be analyzed to obtain another measure of the resonator-quality. Since the acoustic mirrors are Bragg reflectors, it is expected that the decay underneath the mirror follows an exponential. The exponential decay rate can serve as an indicator of the mirror quality. To investigate this, the following procedure is applied to each displacement map:

1. The decay underneath the left mirror is examined by selecting slices. For the x-range of the slices, both the left mirror and the IDT (uninterrupted) are selected. For the y-range, the regions of maximum displacement are selected. For samples B35 and B100, this corresponds to one continuous region. For sample B50, this corresponds to two separate regions.

2. All slices belonging to a certain maximum along the x-axis, are averaged along the y-direction.

3. The slice(s) is/are interpolated. The result is a decaying wave pattern.

4. The peaks are selected.

5. The peaks are plotted.

6. An exponential is fitted to the curve consisting of peaks.

7. The steps above are repeated for the right mirror.

The steps above were applied to the displacement maps shown in Figs. 5.3 (B35), 5.4 (B50), and 5.5 (B100). The displacement in resonator B35 was to small to allow for fitting, therefore these results are not presented.
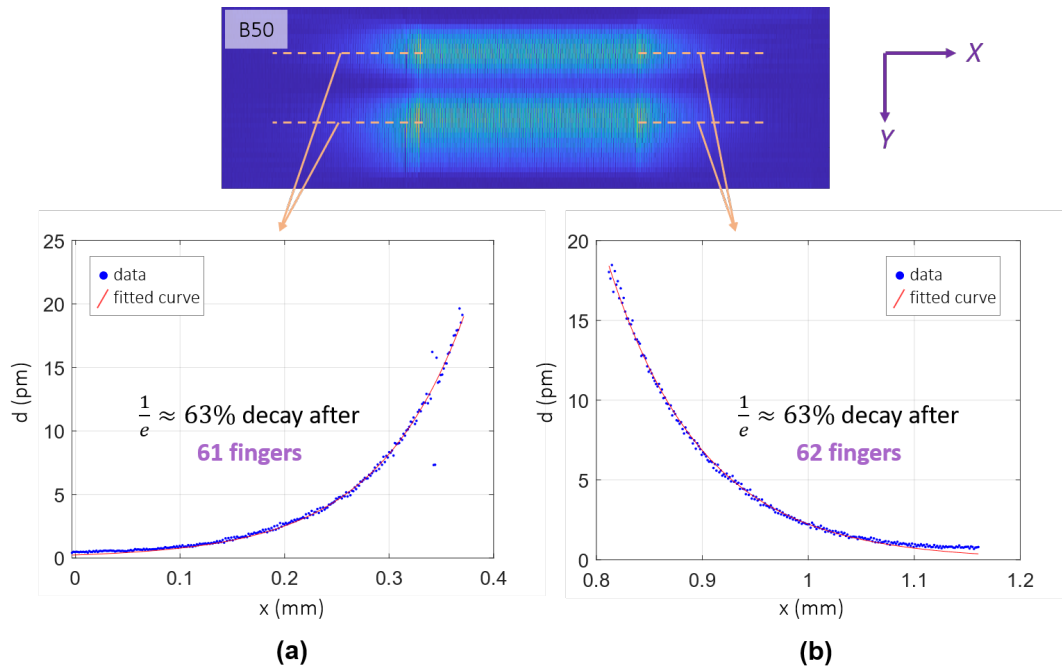
Figure 5.7: Exponential decay underneath the mirrors of sample B50. The map at the top corresponds to Fig. 5.4. The data points in graphs **(a)** and **(b)** represent the interpolated peaks of the decaying wave pattern underneath the mirrors (and IDT). An exponential is fitted to the data points. For the left mirror, the wave displacement has decayed by a factor e after penetrating approximately 61 mirror fingers ($\approx 84.4\ \mu m$). For the right mirror, the same decay has occurred after penetrating approximately 62 mirror fingers ($\approx 86.8\ \mu m$).

Figure 5.8: Exponential decay underneath the mirrors of sample B100. The map at the top corresponds to Fig. 5.5. The data points in graphs **(a)** and **(b)** represent the interpolated peaks of the decaying wave pattern underneath the mirrors (and IDT). An exponential is fitted to the data points. For the left mirror, the wave displacement has decayed by a factor e after penetrating approximately 68 mirror fingers ($\approx 95.2\ \mu m$). For the right mirror, the same decay has occurred after penetrating approximately 62 mirror fingers ($\approx 86.8\ \mu m$).

The fitting function used in Figs. 5.7 and 5.8 is $d = ae^{bx}$. The following values for the absolute decay are found:

$$|b|_{B50,left} = 11.72\,\text{mm}^{-1} \quad |b|_{B50,right} = 11.59\,\text{mm}^{-1}$$
$$|b|_{B100,left} = 10.44\,\text{mm}^{-1} \quad |b|_{B100,right} = 11.60\,\text{mm}^{-1} \tag{5.5}$$

The decay rate underneath the left mirror differs significantly between samples B50 and B100. On the other hand, the decay rate associated with the right mirror is roughly the same for both samples. The decay rate for the right mirror is more straightforward to interpret as only the mirror is involved. The decay underneath the left mirror also includes the section underneath the IDT. Recall that the mirror and IDT were not perfectly adjacent to one another, but that there was a small gap. The effect of this geometry on the operation of the mirror is unclear. Therefore, the decay rate underneath the left mirror less meaningful compared to the decay rate underneath the right mirror.

From theory it follows that the degree of loss associated with scattering into BAWs increases with increase in metal thickness. This theoretical fact in combination with the observation that the decay rates underneath the right mirrors are the same for samples B50 and B100, leads to the conclusion that the reflectivity of the right mirror in B100 is less than the reflectivity of the same mirror in B50. If the reflectivity would be the same or higher for B100, the observed decay rate would be faster.

5.4 Measurement results: Conclusion

The goal of fabricating and measuring samples B35, B50, and B100 was making a statement about the influence of metal thickness on the finesse. The analysis of the acoustic resonance spectra (Sec. 5.2) indicates that for all three resonators, the actual finesse is significantly lower than the finesse based on the assumption of no loss. Moreover, there is an increase in finesse between B35 and B50. However, the finesse remains more or less constant between B50 and B100. The first hypothesis explaining this observation, is that from 35 nm to 50 nm the increase in reflectivity exceeds the increase in mirror-associated loss, but that from 50 nm to 100 nm, these two effects cancel out. Another possible explanation is that the total propagation loss limits a considerable increase in finesse beyond 50 nm.

The analysis of the displacement maps, specifically the exponential decay underneath the mirrors (Sec. 5.3.2), suggests that the mirror reflectivity (without taking loss into account) is lower for B100 compared to B50. The resultant reflectivity (taking loss into account) is believed to be the same because the exponential decay rate is identical, while the mirror-associated loss is higher for B100 according to theory.

There is no possibility of combining the hypotheses from the different measurement results. More data is required to make any conclusive statements.

Chapter 6

Conclusion and Outlook

This thesis was aimed at developing surface acoustic wave (SAW) resonators that are suitable for optically detecting electrically excited phonons, and maximizing their finesse by altering the metal thickness. The prospective aim of this project is to optically detect thermal phonons, but since the displacement associated with thermal phonons is very small (0.5 - 5.0 fm, depending on the resonator size), a realistic first goal was to detect electrically excited phonons (10 - 100 pm, depending on the resonator size). Acoustic resonators are an interesting topic of study because of their promising role in quantum technology: single phonons can function as carriers of quantum information, and their confinement in acoustic resonators allows for interaction with two-level systems such as quantum dots.

The displacement of phonons in acoustic resonators can be measured with a variety of methods; for this research a fiber-based scanning Michelson interferometer was used. The electronic noise-level of this setup (roughly 25 fm) exceeds the signal of thermal phonons, but electrically excited phonons can be measured. Two types of measurements can be obtained with the interferometer: acoustic resonance spectra and displacement maps. In chapter 3, both types of measurements were performed on a generic acoustic resonator consisting of two acoustic mirrors and two IDTs. From the acoustic resonance spectra it became apparent that the presence of peaks is highly dependent on the exact position of the focused laser beam at the time of measurement. To obtain a complete spectrum, the measurement has to be repeated over a range of x-positions and all results have to be combined into a single spectrum. Moreover, the displacement maps clearly indicated the presence of standing waves and thereby the workings of the resonator and interferometer were confirmed.

In chapter 4, the fabrication process of SAW resonators was detailed, and the requirements for a "good" resonator were listed. For this thesis, all resonators are aluminum on GaAs and they were fabricated using electron-beam lithography and electron-beam metal evaporation. In the context of this thesis, a "good" resonator allows for optical probing and has a relatively high finesse ($\mathcal{F} > 100$). The finesse can be optimized by altering the choice and thickness of metal. The exact relation between mirror reflectivity (or finesse) and aluminum thickness is unknown. However, according to theory, both the reflectivity and scattering into bulk acoustic waves (BAWs) by the mirrors, increases as the metal thickness is increased.

The relation between aluminum thickness and finesse was experimentally investigated in chapter 5, where three samples that are identical in design, apart from their aluminum thickness, were introduced. The maximum finesse obtained was $\mathcal{F} \approx 11$ for the 100 nm resonator. For all three resonators, the acoustic resonance spectra and displacement maps were measured. From the resonance spectra, it followed that the free spectral range increased – and therefore the effective length decreased – with metal thickness. Moreover, the values for the finesse for all three resonators were considerably lower than the values expected in a lossless scenario. Apparently, in the current de-

sign losses play a non-negligible role and therefore they need to be taken into account. There was an increase in finesse from 35 nm to 50 nm of aluminum, but the finesse remained roughly the same from 50 nm to 100 nm. Evidently, the mirror reflectivity increases between 35 nm and 50 nm. For the constant finesse from 50 nm to 100 nm there are two possible explanations: either the increase in mirror mass leads to an increase in reflectivity that is (roughly) compensated for by an increase in scattering into BAWs (loss), or the propagation loss limits a significant increase in finesse beyond 50 nm. Additionally, an analysis of the displacement maps led to the hypothesis that the mirror reflectivity decreased between 50 nm and 100 nm. This could explain the observation that the decay rate of the displacement underneath the mirrors is practically identical for 50 nm and 100 nm, despite the expectation that more SAWs are converted into BAWs for the 100 nm resonator.

The three hypotheses mentioned above cannot be fully united. More experiments are required to uncover the true relation between finesse, reflectivity, loss, and metal thickness. One such experiment is reducing the effect of the propagation loss by decreasing the resonator length. The propagation loss that is hypothesized to limit an increase in finesse, depends on both the round-trip propagation loss and on the number of round-trips, and therefore on the finesse. The round-trip propagation loss can be limited by reducing the mirror separation. A noteworthy added advantage of decreasing the resonator length, is the fact that the displacement associated with the phonons will increase. A follow-up experiment could be designed as follows: using the method presented in Sec. 4.2.1 resonators like the three presented in chapter 5 could be fabricated, but with the IDT directly adjacent to the mirror. Then, the resonator length could be shortened to about 10 µm. For this configuration, a multitude of resonators could be produced with different thicknesses. When using the same thicknesses as presented in this thesis (35 nm, 50 nm, and 100 nm), it can be checked whether the propagation loss was indeed the limiting factor. Another design improvement that can be made, is incorporating curved mirrors that match the spatial profile of the wavefront of the acoustic field, this would further limit loss.

Once the optimal aluminum thickness has been found, and enhancements such as reduced resonator length and curved mirrors have been incorporated, steps towards the detection of thermal phonons can be made. As was mentioned in Sec. 3.3, the electronic noise level of the Michelson interferometer exceeds the displacement level associated with thermal phonons. The aforementioned design improvements to enhance the resonator-finesse and the addition of a lock-in amplifier to the setup are not likely to overcome this issue. Therefore, it is necessary to switch to another optical measurement technique: an open microcavity. Not only the acoustic resonator, but also the optical detection setup can be associated with a finesse. A Michelson interferometer has a finesse of 1, whereas the finesse of the open microcavity made specifically for this project is 2000. This increase in finesse will increase the signal-to-noise ratio by a factor of 2000 as well and should allow for the detection of thermal phonons. When using the open microcavity, the resonators need to be fabricated on coated GaAs (GaAs-AlGaAs) that functions as a Bragg reflector. Preliminary tests have already shown that producing samples on this substrate requires no alterations in the fabrication process.

Lastly, it needs to be mentioned that many more intriguing experiments can be performed with IDTs and acoustic mirrors, see Fig. 6.1. Earlier in this thesis, the analogy between acoustic resonators and optical cavities was mentioned. During this project, a sample consisting of 4 IDTs was produced to investigate whether interference patterns similar to those in optics can be produced. Moreover, a sample consisting of two IDTs and a slanted mirror has been fabricated with the idea that it will act as a SAW beam splitter due to symmetry of the GaAs crystal. Measurements on both samples still need to be performed, but they illustrate the variety of systems that can be created.
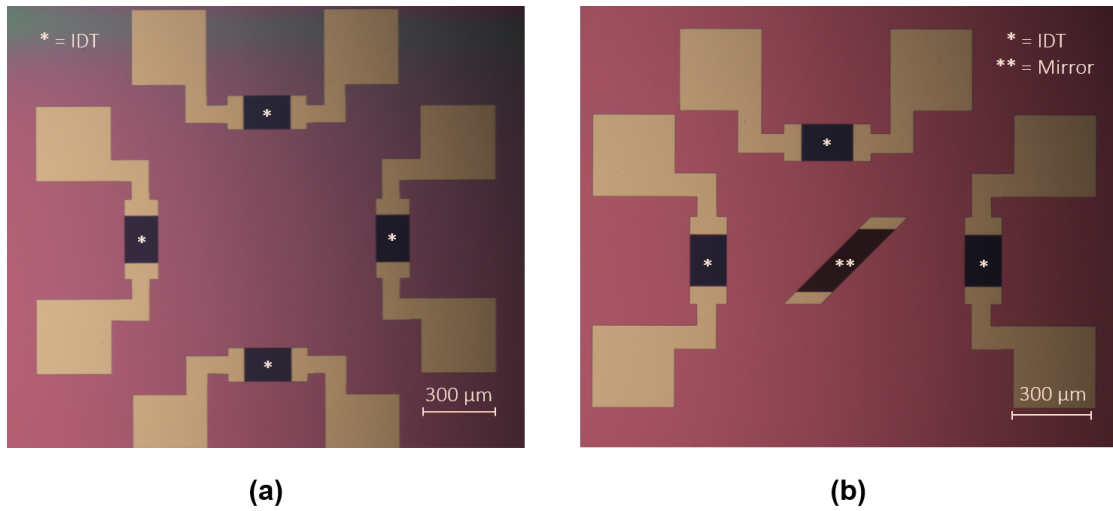
Figure 6.1: 4 IDTs in square arrangement and a SAW beam splitter (a): A sample consisting of 4 IDTs ($N_f = 50$) in a square configuration. By exciting several IDTs at once, it can be investigated whether interference patterns emerge. **(b)**: A sample consisting of 3 IDTs ($N_f = 50$) and an acoustic mirror ($N_m = 100$) slanted at 45 degrees. It is suspected that the slanted mirror might act as an acoustical beam splitter. Both images were taken after the developing step in the fabrication process.

Appendix A

List of Samples

Data directories of all samples:

- **A**: \\data03\pi-loeffler\00-projects\quantum-acoustics\IDT_samples\2022_Samples Thomas\Succesful Samples\1 GHz\2022111_1GHz cavity

- **B35**: \\data03\pi-loeffler\00-projects\quantum-acoustics\IDT_samples\2022-2023 Samples Yasmin\Successful Samples\20230209_Resonator_1IDT_Nf10_Nm250_IDTNextToMirror_35Al

- **B50**: \\data03\pi-loeffler\00-projects\quantum-acoustics\IDT_samples\2022-2023 Samples Yasmin\Successful Samples\20230210_Resonator_1IDT_Nf10_Nm250_IDTNextToMirror_50Al

- **B100**: \\data03\pi-loeffler\00-projects\quantum-acoustics\IDT_samples\2022-2023 Samples Yasmin\Successful Samples\20230224_Resonator_1IDT_Nf10_Nm250_IDTNextToMirror_100Al

- **2 IDTs**: \\data03\pi-loeffler\00-projects\quantum-acoustics\IDT_samples\2022-2023 Samples Yasmin\Successful Samples\20230104_resonator_2IDT_Nf2_Nm250_Al

- **4 IDTs**: \\data03\pi-loeffler\00-projects\quantum-acoustics\IDT_samples\2022-2023 Samples Yasmin\4 IDTs

- **Beam splitter**: \\data03\pi-loeffler\00-projects\quantum-acoustics\IDT_samples\2022-2023 Samples Yasmin\Beam splitter

- **Proximity test I**: \\data03\pi-loeffler\00-projects\quantum-acoustics\IDT_samples\2022-2023 Samples Yasmin\Failed Samples\20230203_Resonator_1IDT_Nf4_Nm250_IDTNextToMirror

- **Proximity test II**: \\data03\pi-loeffler\00-projects\quantum-acoustics\IDT_samples\2022-2023 Samples Yasmin\Failed Samples\20230207_Resonator_1IDT_Nf4_Nm250_IDTNextToMirror

- **IDTs coated I**: \\data03\pi-loeffler\00-projects\quantum-acoustics\IDT_samples\2022-2023 Samples Yasmin\Successful Samples\20230124_c_2IDT_Nf50_AgAu_BROKEN

- **IDTs coated II**: \\data03\pi-loeffler\00-projects\quantum-acoustics\IDT_samples\2022-2023 Samples Yasmin\Successful Samples\20230216_c_2IDTs_Nf50_BROKEN

Sample name	Sample code	Description	Chapter	Notes
A	2022111_1GHz cavity	Two acoustic mirrors (both $N_m = 250$) and two IDTs (both $N_f = 10$) in between the mirrors, $L = 417$ µm, 5 nm Ti/ 60 nm of Al/ 5 nm of Ti	Chapter 3	Fabricated by Thomas Steenbergen
B35	20230209_Resonator _1IDT_Nf10_Nm250_ IDTNextToMirror_35Al	Two acoustic mirrors (both $N_m = 250$) and one IDT ($N_f = 10$) close to the left mirror, $L = 440$ µm, 35 nm of Al	Chapter 5	On the same substrate tests (among others Figs. 4.2 (c.ii) - (c.iv)) are performed
B50	20230210_Resonator _1IDT_Nf10_Nm250_ IDTNextToMirror_50Al	Two acoustic mirrors (both $N_m = 250$) and one IDT ($N_f = 10$) close to the left mirror, $L = 440$ µm, 50 nm of Al	Chapter 5	
B100	20230224_Resonator _1IDT_Nf10_Nm250_ IDTNextToMirror_100Al	Two acoustic mirrors (both $N_m = 250$) and one IDT ($N_f = 10$) close to the left mirror, $L = 440$ µm, 100 nm of Al	Chapter 5	
2 IDTs	20230104_resonator _2IDT_Nf2_Nm250_ Al	Two acoustic mirrors (both $N_m = 250$), one IDT ($N_f = 2$) in between mirrors and one IDT ($N_f = 2$) outside the mirrors, $L = 417$ µm, 35 nm of Al	Not mentioned in thesis	Measurement of the S_{11} parameter showed nothing, $N_f = 2$ might be too little
4 IDTs	4 IDTs	Square configuration of 4 IDTs ($N_f = 50$), separation between opposite IDTs is 905 µm, 5 nm Cr/ 30 nm Au	Conclusion and Outlook	No measurement results
Beam splitter	Beam splitter	Three IDTs ($N_f = 50$) placed with 90 degree rotation w.r.t. each other, one 45 degree slanted acoustic mirror ($N_m = 100$) halfway between (385 µm) two of the IDTs, 65 nm Al	Conclusion and Outlook	No measurement results
Proximity test I	20230203_Resonator _1IDT_Nf4_Nm250_ IDTNextToMirror	Two acoustic mirrors (both $N_m = 250$) and one IDT ($N_f = 4$) directly adjacent to the left mirror, $L = 440$ µm	Chapter 4	Sample failed at developing stage because structures merged (see Fig. 4.2 (a.ii))
Proximity test II	20230207_Resonator _1IDT_Nf4_Nm250_ IDTNextToMirror	Two acoustic mirrors (both $N_m = 250$) and one IDT ($N_f = 4$) directly adjacent to the left mirror, slanted busbar of left mirror, $L = 440$ µm	Chapter 4	Sample failed at developing stage because structures merged (see Fig. 4.2 (b.ii))
IDTs, coated I	20230124_c_2IDT_ Nf50_AgAu_ BROKEN	Two IDTs ($N_f = 50$), $L = 700$ µm, fabricated on coated GaAs, 5 nm Ag/ 60 nm Au	Conclusion and Outlook	Broke while aligning in open-microcavity
IDTs, coated II	20230216_c_2IDTs_ Nf50_ BROKEN	Two IDTs ($N_f = 50$), $L = 700$ µm, fabricated on coated GaAs, 60 nm Ag	Conclusion and Outlook	Broke while aligning in open-microcavity

Acknowledgements

I had a truly great time working on this project and there are many people who contributed to this! First of all, I would like to thank Matteo for answering my hundreds of questions (always with lots of enthusiasm), teaching me everything about the setup and more, and the fun times we had. Also, I would like to thank Wolfgang for all the exciting conversations, pleasant supervision, and trust in me. Both Matteo and Wolfgang have provided with great guidance during these months, which made coming to university very enjoyable and pleasant. Not to forget, Thomas worked on the project before me and spent a lot of time sharing his knowledge with me. I very much appreciated our discussions! To the entire Quantum Optics group: thank you for welcoming on the ninth floor and creating the comfortable work environment which I very much enjoyed. Not only on the ninth floor, but also in the clean room I got great help from Luc Wigbout and Douwe Scholma when learning how to fabricate samples.

Finally, I would like to thank all my friends at university (Rastko, Benjamin, Benjamin, Jeger, Jesse, Vincent, Lindsay, and Matthijs) for making my time at university much more lively. And not to forget, a special thanks to my family and friends outside of university who are always interested in my studies and projects, and therefore have very patiently listened to stories about 'miniature earthquakes' and 'strips of metal that are thinner than bacteria'.

Bibliography

[1] Royer, D. & Dieulesaint, E. *Elastic Waves in Solids I: Free and Guided Propagation* (Heidelberg: Springer Berlin, 1996).

[2] Ilyin, D. A Rayleigh wave/ surface acoustic wave (SAW). `"https://commons.wikimedia.org/wiki/File:Rayleigh_wave.svg"` (2020, retrieved: may 2023).

[3] Mandal, D. & Banerjee, S. Surface Acoustic Wave (SAW) Sensors: Physics, Materials, and Applications. *Sensors* **22**, 820 (2022).

[4] Chen, P., Li, G. & Zhu, Z. Development and application of Saw Filter. *Micromachines* **13**, 656 (2022).

[5] Weiss, M., Wigger, D., Nägele, M., Müller, K., Finley, J. J., Kuhn, T., Machnikowski, P. & Krenner, H. J. Optomechanical wave mixing by a single quantum dot (2021).

[6] Gustafsson, M. V., Aref, T., Kockum, A. F., Ekström, M. K., Johansson, G. & Delsing, P. Propagating phonons coupled to an artificial atom. *Science* **346**, 207 (2014).

[7] Schuetz, M. J. A., Kessler, E. M., Giedke, G., Vandersypen, L. M. K., Lukin, M. D. & Cirac, J. I. Universal Quantum Transducers Based on Surface Acoustic Waves. *Phys. Rev. X* **5**, 031031 (2015).

[8] Chu, Y., Kharel, P., Renninger, W. H., Burkhart, L. D., Frunzio, L., Rakich, P. T. & Schoelkopf, R. J. Quantum acoustics with superconducting qubits. *Science* **358**, 199 (2017).

[9] Takada, S., Edlbauer, H., Lepage, H. V., Wang, J., Mortemousque, P.-A., Georgiou, G., Barnes, C. H. W., Ford, C. J. B., Yuan, M., Santos, P. V., Waintal, X., Ludwig, A., Wieck, A. D., Urdampilleta, M., Meunier, T. & Bäuerle, C. Sound-driven single-electron transfer in a circuit of coupled quantum rails. *Nature Communications* **10** (2019).

[10] Delsing, P., Cleland, A. N., Schuetz, M. J. A., Knörzer, J., Giedke, G., Cirac, J. I., Srinivasan, K., Wu, M., Balram, K. C., Bäuerle, C., Meunier, T., Ford, C. J. B., Santos, P. V., Cerda-Méndez, E., Wang, H., Krenner, H. J., Nysten, E. D. S., Weiss, M., Nash, G. R., Thevenard, L., Gourdon, C., Rovillain, P., Marangolo, M., Duquesne, J.-Y., Fischerauer, G., Ruile, W., Reiner, A., Paschke, B., Denysenko, D., Volkmer, D., Wixforth, A., Bruus, H., Wiklund, M., Reboud, J., Cooper, J. M., Fu, Y., Brugger, M. S., Rehfeldt, F. & Westerhausen, C. The 2019 surface acoustic waves roadmap. *Journal of Physics D: Applied Physics* **52**, 353001 (2019).

[11] Dumur, Ã., Satzinger, K., Peairs, G., Chou, M.-H., Bienfait, A., Chang, H.-S., Conner, C., Grebel, J., Povey, R., Zhong, Y. & Cleland, A. Quantum communication with itinerant surface acoustic wave phonons. *npj Quantum Information* **7** (2021).

[12] Royer, D. & Dieulesaint, E. *Elastic Waves in Solids II: Generation, Acousto-optic Interaction, Applications* (Heidelberg: Springer Berlin, 1999).

[13] Holmgren, O., Knuuttila, J. V., Makkonen, T., Kokkonen, K., Plessky, V. P., Steichen, W., Solal, M. & Salomaa, M. M. Imaging surface-acoustic fields in a longitudinal leaky wave resonator. *Applied Physics Letters* **86**, 024101 (2005). https://doi.org/10.1063/1.1849814.

[14] Msall, M. E. & Santos, P. V. Focusing Surface-Acoustic-Wave Microcavities on GaAs. *Phys. Rev. Appl.* **13**, 014037 (2020).

[15] Takahashi, H., Omori, T. & ya Hashimoto, K. Development of a high-speed, phase-sensitive laser probe system for RF surface acoustic wave/bulk acoustic wave devices with an absolute vibration amplitude measurement function. *Japanese Journal of Applied Physics* **60**, SDDC10 (2021).

[16] Nicolas, J., Reusch, T., Osterhoff, M., Sprung, M., Schülein, F., Krenner, H., Wixforth, A. & Salditt, T. Time-resolved coherent X-ray diffraction imaging of surface acoustic waves. *Journal of Applied Crystallography* **47** (2014).

[17] Hanke, M., Ashurbekov, N., Zatterin, E., Msall, M., Hellemann, J., Santos, P., Schulli, T. & Ludwig, S. Scanning X-Ray Diffraction Microscopy of a 6-GHz Surface Acoustic Wave. *Phys. Rev. Appl.* **19**, 024038 (2023).

[18] Rummel, B. D., Miroshnik, L., Patriotis, M., Li, A., Sinno, T. R., Henry, M. D., Balakrishnan, G. & Han, S. M. Imaging of surface acoustic waves on GaAs using 2D confocal Raman microscopy and atomic force microscopy. *Applied Physics Letters* **118**, 031602 (2021).

[19] Hellemann, J., Müller, F., Msall, M., Santos, P. V. & Ludwig, S. Determining Amplitudes of Standing Surface Acoustic Waves via Atomic Force Microscopy. *Phys. Rev. Appl.* **17**, 044024 (2022).

[20] Babic, D. & Corzine, S. Analytic expressions for the reflection delay, penetration depth, and absorptance of quarter-wave dielectric mirrors. *IEEE Journal of Quantum Electronics* **28**, 514 (1992).

[21] Steenbergen, T. *The Generation and Measurement of SAWs*. Msc thesis, Leiden University (2023).

[22] Delft University of Technology. *Noise in Harmonic Osillators in 'Open Quantum Sensing and Measurement Notes'* (https://qsm.quantumtinkerer.tudelft.nl/3_noise_in_HOs/, retrieved: June 30, 2023).

[23] Hauer, B., Doolin, C., Beach, K. & Davis, J. A general procedure for thermomechanical calibration of nano/micro-mechanical resonators. *Annals of Physics* **339**, 181 (2013).

[24] Kelly, L., Berini, P. & Bao, X. Measuring Velocity, Attenuation, and Reflection in Surface Acoustic Wave Cavities Through Acoustic Fabry Pérot Spectra. *IEEE Transactions on Ultrasonics, Ferroelectrics, and Frequency Control* **69**, 1542 (2022).

[25] Reuble, M. *Creating and Imaging Surface Acoustic Waves on GaAs*. Msc thesis, Queen's University (2009).